UTILIZATION OF GRAPHENE AND MOS$_2$ FOR VOLATILE ORGANIC COMPOUND SENSOR APPLICATIONS

A Thesis Submitted to
the Graduate School of
İzmir Institute of Technology
in Partial Fulfillment of the Requirements for the Degree of

MASTER OF SCIENCE

in Chemistry

by
Tuna DURAN

July 2023
İZMİR

We approve the thesis of **Tuna DURAN**

Asst. Prof. Dr. Onur BÜYÜKÇAKIR
Department of Chemistry, İzmir Institute of Technology

Prof. Dr. Hasan ŞAHİN
Department of Photonics, İzmir Institute of Technology

Assoc. Prof. Dr. Mehmet YAĞMURCUKARDEŞ
Department of Photonics, İzmir Institute of Technology

Assoc. Prof. Dr. Serkan ATEŞ
Department of Physics, İzmir Institute of Technology

Assoc. Prof. Dr. Ümit AKINCI
Department of Physics, Dokuz Eylül University

4 July 2023

Asst. Prof. Dr. Onur Büyükçakır
Supervisor, Department of Chemistry
İzmir Institute of Technology

Prof. Dr. Hasan Şahin
Co-Supervisor, Department of Photonics
İzmir Institute of Technology

Prof. Dr. Gülşah ŞANLI-MOHAMED
Head of the Department of
Chemistry

Prof. Dr. Mehtap EANES
Dean of the Graduate School of
Engineering and Sciences

ACKNOWLEDGMENTS

I want to express my heartfelt gratitude to Prof. Dr. Hasan Şahin, my co-supervisor, for his invaluable advice, guidance, and unwavering patience during my master's education. Working under his mentorship has been an incredibly enriching experience for me. I would also like to extend my thanks to Asst. Prof. Dr. Onur Büyükçakır, my supervisor, for his unconditional support and assistance throughout my research.

I am deeply grateful to my thesis committee members, Assoc. Prof. Dr. Serkan Ateş and Assoc. Prof. Dr. Ümit Akıncı, for dedicating their time and actively participating in the evaluation of my work.

Special regards go to my mentors and friends, Mehmet Yağmurcukardeş, Yiğit Sözen, Anılcan Kuş, and Mehmet Başkurt, for their continuous support. It has been a pleasure collaborating with each of you.

I would also like to extend my appreciation to my friends Mert Kurak, Fırat Tan, Yankı Yayak, Nilüfer Baldır, Ali Cem Demirok, Pınar Öztürk, Ece Topçu, Ferit Begar, Özlem Ersoy, and Ozan Orhan for their unwavering comradery and friendship.

I would like to thank my family, Melek Fitnat Duran, Hacı Mehmet Duran, Hilmi Altınkaya, Hamide Altınkaya, Murat Devrim Altınkaya, Demet Altınkaya, Mehmet Duran, Sadet Duran and for their unconditional love and neverending patience.

Finally, I owe a deep thank to Büşra Buse Tütüncü for her continious love, help and support.

This research was supported by TUBITAK with 120F318 project number.

ABSTRACT

UTILIZATION OF GRAPHENE AND MOS$_2$ FOR VOLATILE ORGANIC COMPOUND SENSOR APPLICATIONS

The novel 2D materials such as graphene and transition-metal dichalcogenides have already shown impressive volatile organic compound (VOC) gas monitoring performances as in sensitivity, limit of detection and response time.

This thesis discusses the experimental-theoretical examination of optical, electronic and morphological properties of novel 2D materials and their utilization in VOC gas sensor field, by means of several characterization techniques and density functional theory (DFT).

Aside from the basic familiarization with the experimental and theoretical methodology in Chapter 2, examination of the functionalization of exfoliated MoS$_2$ using DDT (1-Dodecanethiol) in Chapter 3, which eventually led to a research paper. The DDT treatment is incorporated into the NMP (N-methyl pyrrolidone) exfoliation procedure, resulting in successful functionalization as confirmed by optical, morphological, and theoretical analysis. Raman spectroscopy showed the formation of graphitic species on MoS$_2$ sheets, with decreased sulfur-vacant sites as the DDT ratio increased. STEM and AFM data confirmed the presence of graphitic quantum dots (GQDs) on MoS$_2$ nanosheets, while PL intensities demonstrated significant improvements in photoluminescent properties. This study enhances our understanding of surface and edge chemistry in exfoliated MoS$_2$ and expands the possibilities for broader applications of MoS$_2$ and GQD particles.

Moreover, the attention was drawn to the investigation of the contrasting responses of graphene gas sensors fabricated using different synthesis methods, in the submitted paper explained in Chapter 4. Exfoliated graphene sensors decrease in current when exposed to methanol, while CVD graphene sensors increase in current. The differences in edge site population and electrical properties contribute to these responses. The study provided theoretical and experimental findings for an understanding of the reasons behind the inverse sensor responses of CVD and exfoliated graphene on an atomic scale.

ÖZET

GRAFEN VE MOS$_2$’NİN UÇUCU ORGANİK GAZ SENSÖRÜ UYGULAMALARI İÇİN KULLANILMASI

Grafen ve iki boyutlu geçiş metali dikalkojenit gibi yeni nesil malzemeler, hassasiyet, tespit limiti ve tepki süresi açısından etkileyici uçucu organik bileşik (VOC) gaz izleme performansı sergilemiştir. Bu tez, yeni nesil 2D malzemelerin optik, elektronik ve morfolojik özelliklerinin deneysel ve teorik olarak incelenmesini ve bunların VOC gaz sensörü alanındaki kullanımını, çeşitli karakterizasyon teknikleri ve yoğunluk fonksiyonel teorisi (DFT) aracılığıyla tartışmaktadır.

Çalışmanın ikinci bölümünde, deneysel ve teorik yöntemlere temel bir aşinalık sağlandıktan sonra, üçüncü bölümde ise deneysel veriler ve teorik analizlerle desteklenen, DDT (1-Dodekanetiyol) kullanılarak eksfoliye MoS$_2$’nin fonksiyonelleştirilmesi incelenmiştir. DDT işlemi, NMP (N-metil pirolidon) eksfoliye işlemine entegre edilmiş ve optik, morfolojik ve teorik analizlerle doğrulanmış başarılı bir fonksiyonelleştirme elde edilmiştir. Raman spektroskopisi, MoS$_2$ tabakalarında grafenik türlerin oluşumunu göstermiş ve DDT oranının artmasıyla kükürt boşluklu bölgelerin azaldığını göstermiştir. STEM ve AFM verileri, MoS$_2$ nano levhalarında grafenik kuantum noktalarının (GQD) varlığını doğrulamıştır, PL şiddetleri ise fotolüminesans özelliklerinde önemli iyileştirmelerin olduğunu göstermiştir. Bu çalışma, eksfoliye MoS$_2$’deki yüzey ve kenar kimyasını anlamamıza katkı sağlamış ve MoS$_2$ ve GQD partiküllerinin daha geniş uygulamaları için olanakları genişletmiştir.

Ayrıca, dördüncü bölümde açıklanan gönderilmiş makalede, farklı sentez yöntemleri kullanılarak üretilen grafen gaz sensörlerinin zıt tepkilerinin araştırılmasına odaklanıldı. Eksfoliye grafen sensörleri metanola maruz kaldığında akım azalırken, CVD (Kimyasal Buhar Biriktirme) yöntemiyle üretilen grafen sensörleri akım artışı göstermiştir. Kenar yerleşimlerindeki farklılıklar ve elektriksel özellikler, bu tepkilerin sebeplerine katkı sağlamaktadır. Bu çalışmada, CVD ve eksfoliye grafenin atomik ölçekte zıt sensör tepkilerinin nedenlerinin anlaşılması için deneysel ve teorik bulgular sunulmuştur.

TABLE OF CONTENTS

LIST OF FIGURES

LIST OF TABLES

CHAPTER 1

INTRODUCTION

Chemical sensors have become indispensable tools in various industries, including environmental monitoring, healthcare, and industrial safety. The growing demand for highly sensitive and selective gas sensing devices has driven the exploration of novel materials with exceptional properties. Graphene and molybdenum disulfide (MoS_2) have emerged as promising candidates for gas sensor applications due to their unique characteristics[99].

Graphene, a two-dimensional carbon allotrope, exhibits exceptional electrical, thermal, and mechanical properties. Its high surface-to-volume ratio and excellent electron mobility enable efficient gas molecule adsorption and rapid response to changes in the gas environment. Furthermore, graphene's properties can be tailored through functionalization, allowing for improved gas selectivity and sensitivity[9].

TMDs are group of 2D materials having formula of MX_2, where M stands for transition-metal atoms namely Mo, W, Nb, V, etc., while X stands for chalcogenide atoms, S, Se, or Te. Transition-metal dichalcogenides form X-M-X bonds, creating tetragonal, hexagonal, and rhombohedral geometries with 1T, 2H and 3R phases. Mentioned conformers and stacking orientations give rise to various optic and electronic properties of TMDs due to their charge distributions and interlayer interactions. For instance, the electronic characteristics of TMDs change as semiconducting or metallic, which are also used in different fields by functionalizing with various molecules or structures. Interlayer interactions between TMD layers are dominated by van der Waals interactions which make the exfoliation and functionalization process feasible. Even though, MoS_2 conforms in trigonal prismatic semiconducting 2H phase in standard conditions, in-situ changes in the structure play a key role in the functionalization process. Chemical exfoliation involves initiating butyllithium (n-BuLi) intercalation between MoS_2 layers which leads to the exfoliation of the layers. On the other hand, this process converts structurally 2H-MoS_2 to 1T-MoS_2 due to the electron transfer from n-BuLi to MoS_2[92], as confirmed by zeta-potential measurements, benefiting from changed charge values upon phase change[37]. Methodologies in functionalization of TMD which involve the usage of ce-1T-MoS_2 (chemically-exfoliated)[92]. The authors devised a strategy where they incorporate iodoorganic compounds or diazonium salts[48] on chemically exfoliated MoS_2, WS_2, and $MoSe_2$ nanosheets. It was also reported that for the $MoSe_2$ and WS_2 nanosheets, the yields of the functionalization of MoS_2 are quite

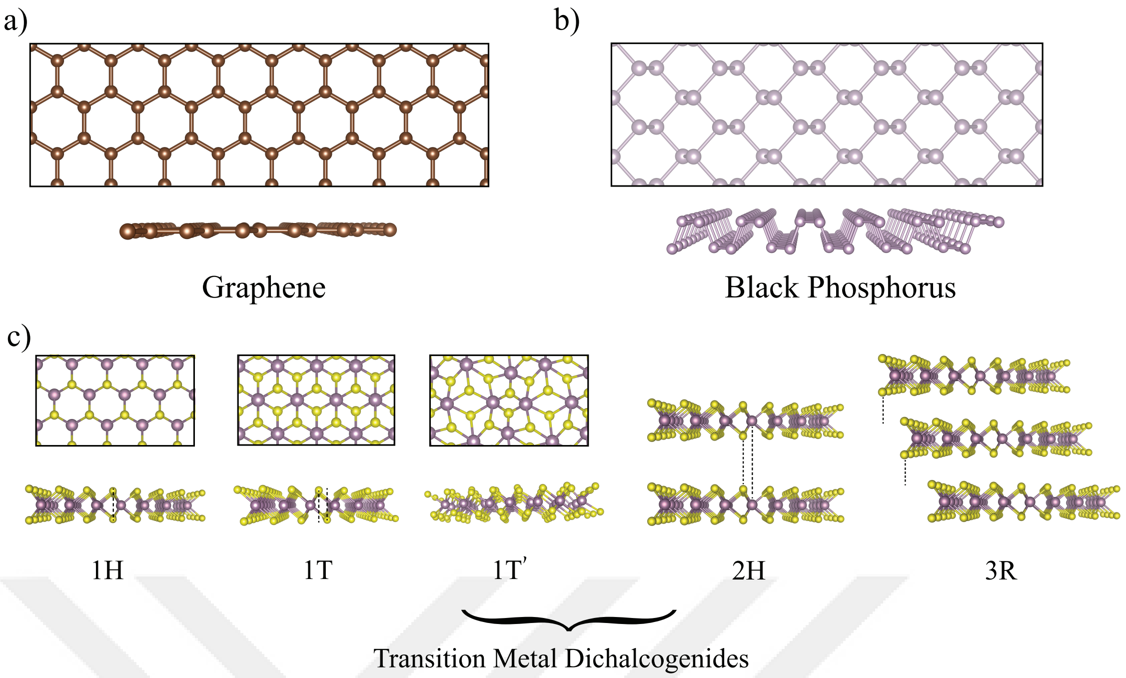

Figure 1.1. Examples of popular 2D materials such as a) graphene, b) black phosphorus and c) molybdenum (IV) disulfide as a model for transition-metal dichalcogenides (TMDs). Different stable phases of MoS_2 and other MX_2 are given.

proximate for MoS_2 functionalization, according to the XPS results. Another type of functionalization involves sulfur conjugation by benefiting from the sulfur vacancies on the basal plane of the TMD layer[18]. On organic functionalization of MoS_2, while the covalent and ligand conjugation functionalization was usually carried out on 1T-MoS_2, coordination-based functionalization was demonstrated by utilizing either sulfur-edged molecules to coordinate with molybdenum or metal-edged molecules to coordinate with sulfide atoms on the surface.

Consequently, following the industrial revolution in a short time, first, microtechnology and then nanotechnology are developing rapidly nowadays. To keep up with this development, materials research at the nanoscale requires the exploration of new materials. Functionalizing techniques can be used by adapting them for nanotechnology. As an alternative and/or successor to graphene, TMDs have been strongly considered as promising materials for sensor applications. For instance, Kim et al. developed a model for a fluorescent sensor to detect Alzheimer's disease by exploiting weak interactions in the WS_2 layer interface, which acted as the fluorescence quencher[46]. They observed that functionalizing WS_2 nanosheets with carboxylic acid dextran or trimethylammonium dextran resulted in 3.6 times faster adsorption rates compared to pristine or phenoxy-

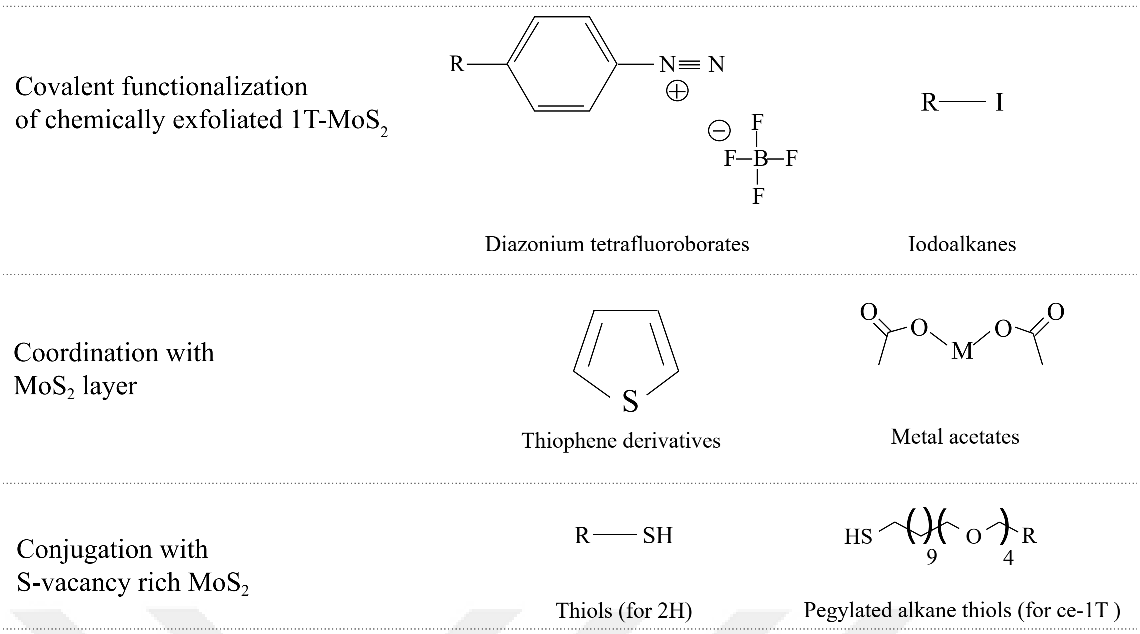

Figure 1.2. Correlation of utilized chemicals and manners of functionalization of TMDs.

dextran functionalized WS_2. Moreover, biosensor designs utilizing a wide range of target molecules have been demonstrated. Yang et al. presented a fluorescent biosensor for the detection of Glycated hemoglobin[100]. The increase in HbA1c concentration led to fluorescence quenching, indicating a general trend. The functionalization of WS_2 with B-PVA through an esterification reaction between polyvinyl alcohol and carboxyphenylboronic acid enabled simultaneous functionalization and exfoliation of WS_2, making it suitable for sensing HbA1c.

MoS_2, a layered transition metal dichalcogenide, possesses remarkable electrical and chemical properties that make it suitable for gas sensing applications. The functionalization of MoS_2 through various methods, including surface modification, doping, and hybridization, can enhance its gas sensing performance by tailoring its band structure and improving charge transfer kinetics[26].

In particular, the functionalization of MoS_2 plays a vital role in optimizing its gas sensing properties. It enables control over the material's surface chemistry, facilitating enhanced gas adsorption and reaction kinetics. Several functionalization strategies have been explored, including the introduction of chemical species such as metal atoms or organic molecules onto the MoS_2 surface. Additionally, the formation of heterostructures with other materials, such as graphene, has been investigated to exploit synergistic effects and create hybrid gas sensing platforms with superior performance[90]. Functionalization is a technique of modifying the surface chemistry of a material, which offers various functions, abilities, and new properties to the material. The technique has been used throughout many fields, including chemistry, physics, materials science, molecular biology, and nanotechnology. Functionalization enables either chemical reaction or adsorption of the functional chemicals onto the surface of a material. Functionalization techniques have been performed in ancient times in various areas and at different eras to decorate materials, either by plating or applying surface treatments[30]. The process contains chemical baths, the use of different powders and lacquer combined with minerals, surface coating, inventive processes and materials to create the appearance of higher-quality materials and adapted to specific requirements[30]. For example, in the third and second millennium BC, ancient civilizations ingeniously employed diffusing bonding to conceal rivets on minor luxury items like cosmetic scrapers and tweezers[29]. Beyond historical contexts, functionalization plays a vital role in animal survival and adaptation within their ecosystems. A fascinating illustration of this phenomenon is seen in animals with stripped fur, which facilitates blending into their environment, allowing them to evade predators and approach prey unnoticed. As such, functionalization techniques are extensively applied across nature and various academic disciplines.

In biosensor technology, TMDs such as MoS_2, WS_2, WSe_2, and $MoSe_2$ have been widely studied due to their biocompatibility, bio-detection without labeling, and ease of fabrication. Unwanted adsorption of ambient species like H_2O, CO, and CO_2 on the sensing area poses a challenge in Field-Effect Transistor (FET) sensor technology. Zhang et al. proposed an eco-friendly approach to mitigate this issue by functionalizing the MoS_2 layer using a DNA tetrahedron and biotin-streptavidin conjugation[103].

The functionalization of TMD nanostructures opens up new and diverse applications in the sensor field. Xia et al. enhanced the performance of exfoliated MoS_2 nanosheets at room temperature by designing a NIR light-activated NO_2 sensor, enriching the sulfur vacancies and functionalizing them with ZnO quantum dots[97]. Functionalizing SV-MoS_2 with ZnO quantum dots led to a 5-fold increase in the sensor response. To address the issues of unstable baseline and poor sensitivity in MoS_2-based H_2 sensors, Gottam et al. developed a composite film of MoS_2-Pt by functionalizing MoS_2 with $H_2PtCl_6 \cdot 6H_2O$ in aqueous phase[32]. The addition of platinum as a catalyst improved the stability of the H_2 sensor, surpassing other metal-sulfide sensors. Sui et al. demonstrated a biosensor model for the sensing of 5-Hydroxymethylcytosine (5hmC) and β-GT activity assessment using WS_2 nanosheets as the photoactive material and boronic acid-functionalized carbon dots as a signal amplifier[86]. Kaur et al. reported a biolayer interferometric in-vitro selection technique (BLI-SELEX) for the detection of E. coli toxin subtypes by immobilizing aptamers onto a chitosan exfoliated nanosheet substrate[45]. Functionalization of TMDs typically involves specific chemical reagents and is limited to chalcogen vacancies on layers due to their chemical stability. Lihter et al. employed electrografting to modify the MoS_2 surface and demonstrated the advantages of electrochemical functionalization using 3,5-bis(trifluoromethyl) benzenediazonium tetrafluoroborate[61].

This thesis aims to provide a thorough understanding of the utilization of graphene and MoS_2 in gas sensor applications, with a specific focus on the functionalization of MoS_2. The thesis explored into the fundamental aspects of gas sensing mechanisms involving these materials, discuss the challenges and opportunities in their integration, and explore recent advancements in functionalization strategies to improve gas sensing performance. By analyzing the existing experimental and theoretical (DFT) data, literature and highlighting the gaps and future research directions, this thesis intends to contribute to the development of next-generation gas sensing technologies[96].

CHAPTER 2

METHODOLOGY

2.1. Experimental Methodology

In this section, a brief introduction is given about the fundamental experimental procedures that were used throughout thesis study.

2.1.1. Wet Transfer Method of CVD-Grown Graphene

In the wet transfer method of chemical vapor deposition (CVD) graphene onto a SiO_2/Si substrate, the process involves multiple steps. Initially, graphene is grown on a copper foil using CVD. To provide support, a polymer layer like poly(methyl methacrylate) (PMMA) is coated onto the graphene-covered copper foil through spin-coating. Subsequently, the copper foil is dissolved using an etchant solution, such as ammonium persulfate or ferric chloride, leaving the graphene layer attached to the PMMA film. The remaining copper is then thoroughly rinsed away.

Afterward, the PMMA/graphene film is carefully transferred onto the prepared and cleaned SiO_2/Si substrate. The film is placed onto the substrate with care, ensuring good contact, and applying heat and pressure if needed to enhance adhesion between the graphene and substrate. Once the transfer is complete, the PMMA layer is typically removed by rinsing it with a solvent like acetone. This step dissolves the PMMA, leaving the transferred graphene on the SiO_2/Si substrate. The substrate, now featuring the transferred graphene, can be further processed or utilized for various applications.

2.1.2. Liquid Phase Exfoliation (LPE)

When ultrasonic sound waves propagate through liquid media, they induce pressure changes that cause vibrations in the surrounding atoms, resulting in the formation of micro-bubbles within the liquid. The process from the expansion of these micro-bubbles due to high and low-pressure cycles to their destabilization and subsequent collapse, releasing

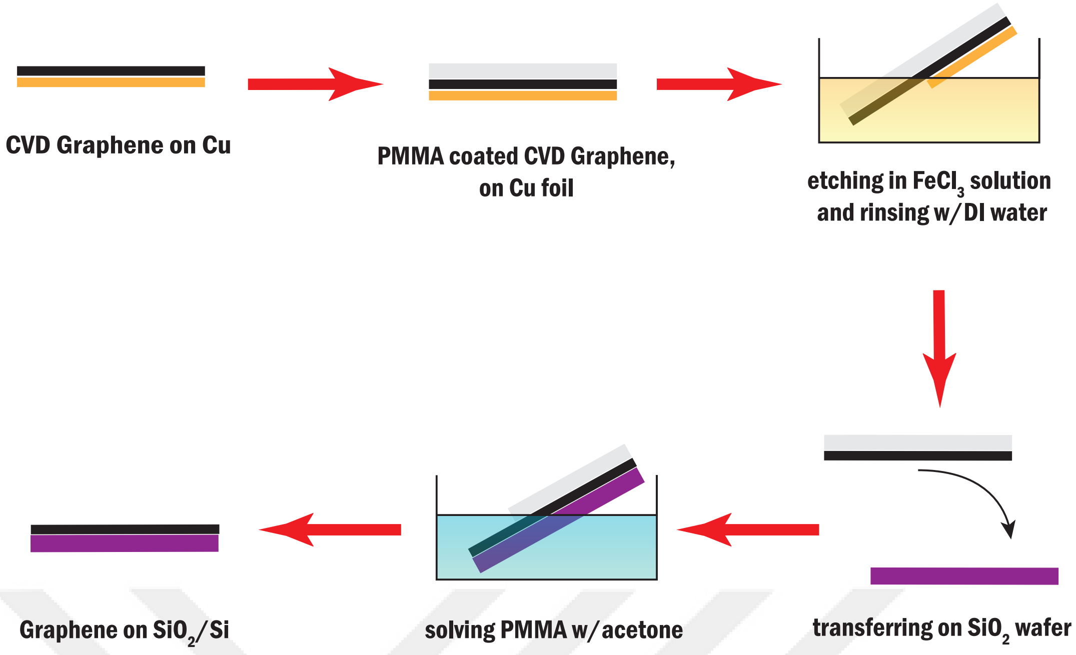

Figure 2.1. The schematic of procedure for wet transfer process of CVD graphene by utilizing PMMA.

a significant amount of energy, is referred to as cavitation. The most significant physical effects include the generation of micro-jets and shear forces resulting from the cavitation-induced high-pressure water streams. These high-pressure flows cause pore formation, surface erosion, and the separation of layers in bulk TMD crystals. The resulting shear force acts to disrupt the van der Waals interactions between the layers, facilitating the exfoliation process.

The efficiency of exfoliation depends on factors such as sonication power, centrifugation speed, and the choice of solvent. The selection of an appropriate solvent is crucial to create an environment during sonication that facilitates the dispersion of exfoliated and stabilized MoS_2 and WS_2. In this regard, solvents such as N-methyl-2-pyrrolidone (NMP), dimethyl sulfoxide (DMSO), dimethylformamide (DMF), and isopropyl alcohol (IPA) have been utilized. The choice of solvents considers their surface tensions. The compatibility between the surface energy of MoS_2 and WS_2 and the surface tensions of the selected solvents plays a crucial role in the exfoliation process, ensuring the effective separation of bulk structures into individual layers. This relationship can be explained using the Gibbs Free Energy formula:

$$\Delta G_{\text{mix}} = \Delta H_{\text{mix}} - T\Delta S_{\text{mix}} \tag{2.1}$$

In Equation (1), ΔH_{mix} represents the enthalpy of mixture, ΔS_{mix} represents the entropy of the mixture, and T is the absolute temperature. According to this formula, for the formation of a mixture, ΔH_{mix} should be smaller than $T\Delta S_{\text{mix}}$. According to the Second Law of Thermodynamics, in all spontaneous processes that increase the entropy of the universe, the Gibbs Free Energy must decrease. Therefore, for the continuous increase in entropy in the universe, the energy flow should be from the system to the surroundings. In reality, the interaction between the "right" solvent and the "right" solute is the key to achieving liquid-phase exfoliation. The Gibbs Free Energy formula is rearranged below to describe the enthalpy change based on the nature of thermodynamic events, considering solute and solvent:

$$\frac{\Delta H_{\text{mix}}}{V_{\text{mix}}} = \frac{2}{T_{\text{bulk}}}(\delta_{\text{solute}} - \delta_{\text{solvent}})^2\phi \tag{2.2}$$

Here, T_{bulk} represents the thickness of flakes, V_{mix} is the volume of the mixture, ϕ is the volume fraction, and δ denotes the surface energies of the solute and solvent. This equation, formulated using the difference in surface tensions of suspension components to minimize the enthalpy of the mixture, is one method used to calculate the enthalpy change in terms of the solubility factor. Another method used to calculate the enthalpy change in terms of solubility factor is the solution of the Hansen equation. The Hansen parameters between the solute and solvent are defined below.

$$\frac{\Delta H_{\text{mix}}}{V_{\text{mix}}} = \phi(1-\phi)[(\delta_{D,\text{solvent}}-\delta_{D,\text{solute}})^2+0.25(\delta_{P,\text{solvent}}-\delta_{P,\text{solute}})^2+0.25(\delta_{H,\text{solvent}}-\delta_{H,\text{solute}})^2] \tag{2.3}$$

Here, δ_D, δ_P, and δ_H represent the atomic dispersive forces, polar molecular forces, and hydrogen bonding solubility parameters, respectively. For successful exfoliation, where the Gibbs Free Energy approaches zero, the Hansen solubility parameters of MoS_2 and WS_2 should be similar to those of the solvents. The solubility parameters of the solvents used in the project, as well as those of the TMD crystals, are presented in Table 2.1.

The liquid phase exfoliation method is used to produce thin layers of graphene or other two-dimensional materials by dispersing bulk materials in a solvent and applying sonication. There are two common sonication methods used in liquid phase exfoliation: probe sonication and bath sonication.

Probe sonication involves the use of a probe or tip that is immersed in the liquid

Table 2.1. Solubility Parameters of Solvents and TMD Crystals.

Solute/solvent	δD [MPa$^{1/2}$]	δP [MPa$^{1/2}$]	δH [MPa$^{1/2}$]
NMP	18	12.3	7.2
DMF	17.4	13.7	11.3
DMSO	18.4	16.4	10.2
IPA	15.8	6.1	16.4
MoS_2	17.8	9	7.5
WS_2	18	8	7.5

sample. The probe emits high-frequency sound waves that create intense vibrations in the solvent, causing the exfoliation of the layered materials. The tip is usually placed directly into the sample container, and sonication is carried out for a specified duration. The probe sonicator provides precise control and is suitable for smaller sample volumes.

Bath sonication, on the other hand, involves placing the sample container into a bath filled with a suitable solvent. The bath sonicator produces sound waves that create pressure fluctuations in the liquid, leading to the exfoliation of the layered materials. The entire sample container is subjected to sonication simultaneously. Bath sonication is commonly used for larger sample volumes or when multiple samples need to be processed simultaneously.

In both methods, sonication creates cavitation bubbles in the liquid. The rapid expansion and collapse of these bubbles generate strong shear forces, causing the layers of the material to separate and exfoliate into thinner sheets. The sonication time, power, and solvent choice are important parameters that can affect the degree of exfoliation and the quality of the resulting flakes.

Following sonication, the dispersion is typically centrifuged to separate the exfoliated flakes from the remaining bulk material. The supernatant, containing the dispersed flakes, can be collected for further characterization or deposition onto substrates.

It's worth noting that the choice of solvent and the specific sonication parameters may vary depending on the material being exfoliated and the desired application. Optimization of these parameters is often required to achieve the desired exfoliation quality and yield[71,39].

2.1.3. Functionalization of 2D Materials

In this subsection, summarized information of each type of functionalization techniques is given for the 2D materials.

2.1.3.1. Functionalization of MoS_2

Functionalization of 2D MoS_2 refers to the process of modifying the surface of molybdenum disulfide (MoS_2) flakes with different functional groups or molecules. This modification can alter the properties of MoS_2 and enable various applications in electronics, optoelectronics, catalysis, sensing, and energy storage.

Functionalization methods can be broadly categorized into covalent and non-covalent approaches:

Covalent Functionalization: Covalent functionalization involves forming chemical bonds between MoS_2 and the functional groups. Common covalent functionalization methods include:

a. Chemical Functionalization: MoS_2 can react with chemical reagents, such as diazonium salts or organic thiols, to covalently attach functional groups to its surface. These functional groups can introduce specific properties or enable further modification[67].

b. Plasma Functionalization: Plasma treatment, such as oxygen plasma or nitrogen plasma, can introduce functional groups onto the surface of MoS_2 through chemical reactions. Plasma functionalization offers control over the density and type of functional groups attached[47].

Non-covalent Functionalization: Non-covalent functionalization involves weak interactions, such as van der Waals forces or electrostatic interactions, between MoS_2 and the functional molecules. Common non-covalent functionalization methods include[91]:

a. Physisorption: Functional molecules, such as polymers, small organic molecules, or biomolecules, can adsorb onto the MoS_2 surface through weak van der Waals interactions. This method allows for reversible functionalization and preserves the intrinsic properties of MoS_2[12].

b. π-π Stacking: Aromatic molecules with π-conjugated systems can interact with MoS_2 through π-π stacking interactions. This method can modify the electronic structure of MoS_2 and enhance its optical properties[101].

Functionalization of MoS_2 can provide several benefits, including enhanced stability, improved electrical conductivity, controlled bandgap engineering, increased catalytic activity, and improved sensing capabilities. However, it's important to consider the impact of functionalization on the desired properties and carefully select the functional groups or molecules based on the specific application requirements[56,89].

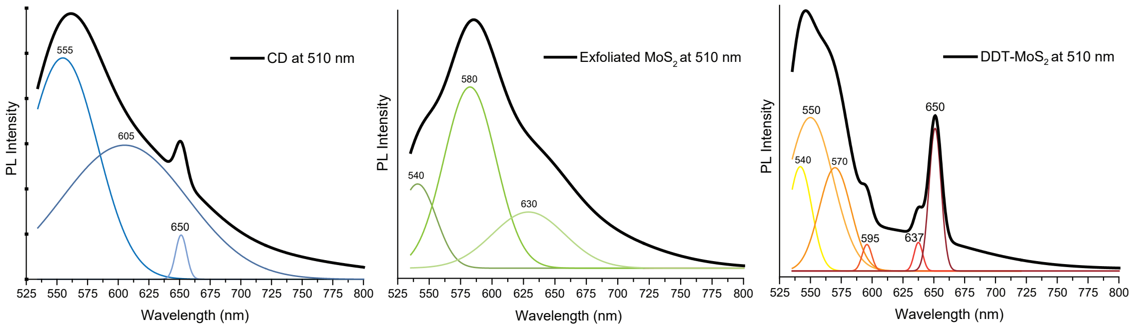

Figure 2.2. The deconvolution of PL data in order to identify different peaks of distinct absorption lines of the investigated 2D material. Plots in figure represent PL data acquired by exciting carbon dots (CD), exfoliated MoS_2 and DDT-functionalized MoS_2 (DDT-MoS_2) samples with 510 nm laser.

2.2. Characterization Techniques

In this section, a brief introduction is given about the fundamental characterization techniques that were used throughout thesis study.

2.2.1. Optical

2.2.1.1. UV-Visible Spectroscopy

UV-Visible spectroscopy is a widely used analytical technique that provides valuable information about the electronic structure and optical properties of materials. It involves the absorption of ultraviolet (UV) and visible (Vis) light by molecules or materials, which leads to electronic transitions between different energy levels.

In UV-Visible spectroscopy, a beam of UV or visible light is directed onto a sample, and the transmitted or reflected light is measured as a function of wavelength. The resulting spectrum provides information about the absorption or reflection properties of the sample over a range of wavelengths. This information can be used to identify and quantify compounds, determine their concentration, investigate electronic transitions, and study the presence of chromophores or conjugated systems.

UV-Visible spectroscopy is particularly useful for characterizing 2D crystals, such as graphene or transition metal dichalcogenides (TMDs), due to their unique electronic properties. It can provide insights into the bandgap, excitonic effects, and charge carrier dynamics of these materials. Additionally, UV-Visible spectroscopy can be used to study the optical properties and stability of functionalized or modified 2D crystals[33,36].

As shown in Fig. 2.2, the DDT-functionalizing of sonicated NMP-MoS_2 sample induced shifts of the original PL peaks, and PL shifts provides hints about changed optic and electronic properties of the sample.

2.2.1.2. Raman Spectroscopy

Raman spectroscopy is a powerful, non-destructive technique for studying the vibrational modes of molecules and materials. It provides information about molecular bonding, crystal structure, and the presence of functional groups. Raman spectroscopy is based on the inelastic scattering of light, where incident photons interact with the sample and undergo a change in energy due to vibrational transitions.

In Raman spectroscopy, a laser beam is focused on the sample, and the scattered light is collected and analyzed. The resulting Raman spectrum represents the intensity of scattered light as a function of energy shift (Raman shift), which corresponds to the vibrational frequencies of the sample. Raman spectroscopy can provide insights into molecular composition, identify chemical species, detect structural defects, and analyze lattice vibrations in materials.

As seen in Fig. 2.3, the shifts of Raman lines that are characteristic to 2D materials, hint on the extrinsic effects on the material that is being analyzed. Therefore, for 2D crystals, Raman spectroscopy is particularly valuable as it can probe the unique phonon modes and structural properties of these materials. It allows for the characterization of layer thickness, strain effects, doping, and interlayer interactions in 2D crystals. Raman spectroscopy is widely used to investigate graphene, TMDs, and other 2D materials, providing valuable information about their structural and electronic properties[25,84].

Raman spectroscopy is also very crucial and well-suited for characterizing 2D materials for the following reasons:

Non-destructive: Raman spectroscopy allows repeated measurements on delicate 2D materials without causing damage.

Structural Information: It provides valuable insights into crystal structure, including layer count, lattice vibrations, and strain effects.

Layer Thickness Determination: Raman spectroscopy enables estimation of layer thickness by analyzing intensity ratios of vibrational modes.

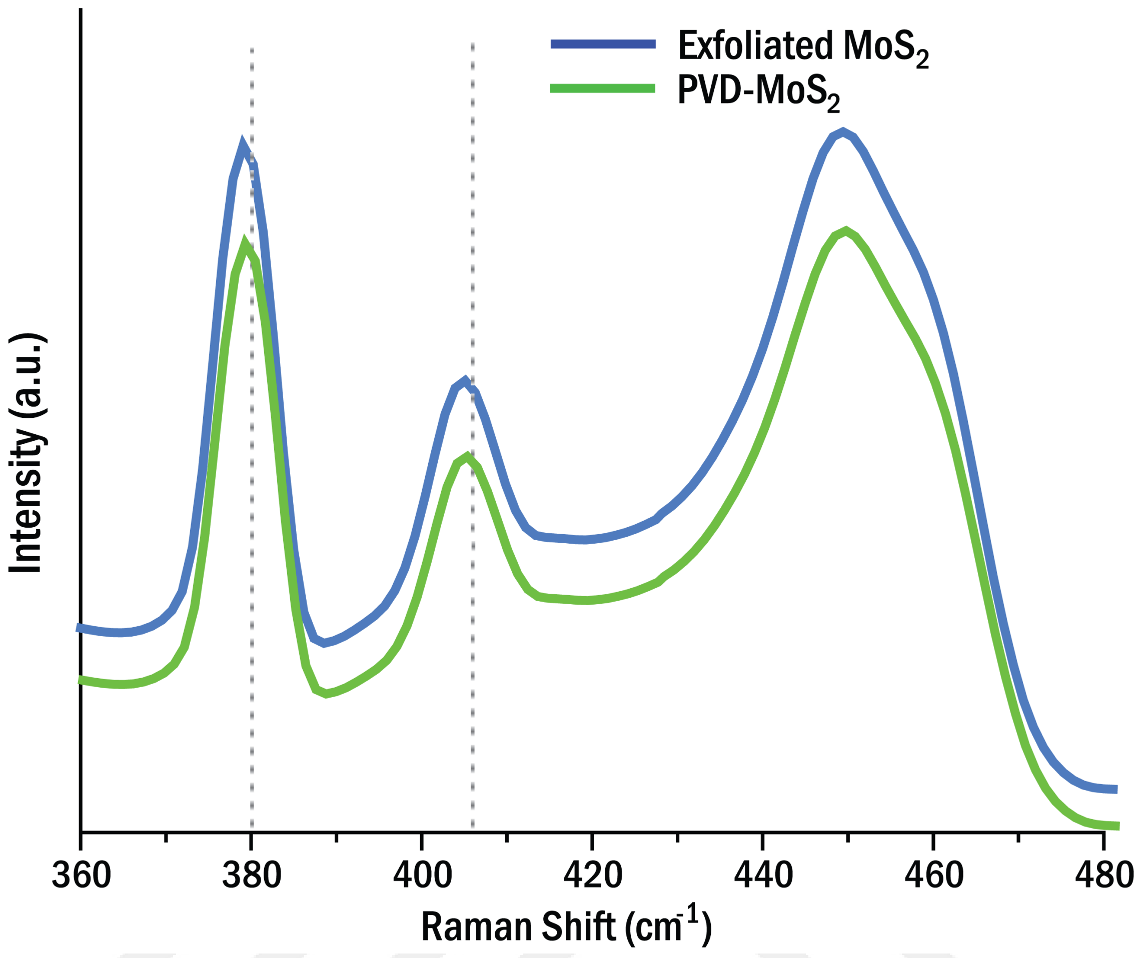

Figure 2.3. Raman spectra of mechanically exfoliated and Physical Vapor Deposited (PVD) MoS_2, excited with 785 nm light source.

Defect and Disorder Analysis: It is sensitive to defects, disorder, and structural imperfections, detected through changes in peak positions, intensities, or the emergence of additional modes.

Phonon Interaction: Raman spectroscopy measures light scattering by phonons, revealing unique phonon modes in 2D materials and their interaction with electronic structure.

Sensitivity to Environmental Effects: It can detect changes in 2D material properties under different environmental conditions, such as temperature, pressure, or gas exposure.

In summary, Raman spectroscopy is a powerful, non-destructive technique providing essential insights into the structural, optical, and electronic properties of 2D materials.

2.2.1.3. Dynamic Light Scattering (DLS)

Dynamic light scattering (DLS), also known as photon correlation spectroscopy or quasi-elastic light scattering, is a technique used to measure the size and diffusion properties of particles or molecules in a solution. It provides information about the hydrodynamic radius or size distribution of particles in the nanometer to sub-micrometer range.

The principle behind DLS is based on the Brownian motion of particles in a fluid. When particles are suspended in a solution, they undergo random thermal motion due to collisions with solvent molecules. This motion is known as Brownian motion. In DLS, a laser beam is directed at the sample, the particles scatter the incident laser light, leading to intensity fluctuations in the scattered light. These fluctuations are caused by the interference of light waves scattered by the particles as they move around randomly[6].

The intensity autocorrelation function, also known as the correlation curve or correlation function, is then calculated from the measured intensity fluctuations. The autocorrelation function provides information about the rate and extent of fluctuations in the scattered light. It can be analyzed using mathematical models, such as the autocorrelation function obtained from the Stokes-Einstein equation, to extract particle size and diffusion properties.

The key concept in DLS is that the speed of Brownian motion is related to the particle size. Smaller particles undergo faster Brownian motion, resulting in quicker intensity fluctuations, while larger particles exhibit slower fluctuations. By analyzing the autocorrelation function, it is possible to determine the diffusion coefficient of the particles, which can be used to calculate their size or size distribution using appropriate mathematical models[11].

2.2.2. Morphological

2.2.2.1. Atomic Force Microscope (AFM)

Atomic Force Microscopy (AFM) is a powerful imaging and characterization technique that allows for high-resolution imaging and analysis of surfaces at the nanoscale. It is widely used in various scientific disciplines, including physics, materials science, biology, and nanotechnology.

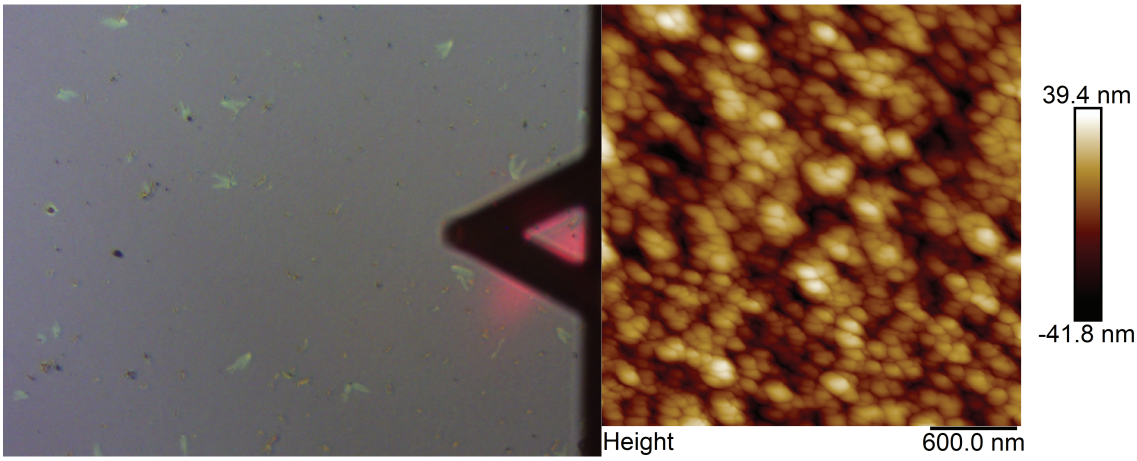

Figure 2.4. The captured Atomic Force Microscope (AFM) images of NMP-exfoliated MoS_2 (NMP-MoS_2) samples on Si/SiO_2. a) General view of surface during cantilever placement part of AFM analysis b) zoomed aggregates of NMP-MoS_2 particles.

AFM operates by using a sharp tip mounted on a cantilever to scan the surface of a sample. The tip is brought into close proximity with the sample, and as the tip scans across the surface, it experiences attractive or repulsive forces between the tip and the atoms or molecules on the sample surface. These forces cause the cantilever to deflect, and the deflection is detected and measured using a laser beam and position-sensitive detectors.

There are several modes of operation in AFM, including contact mode, tapping mode (also known as intermittent contact mode), and non-contact mode. In contact mode, the tip is in constant contact with the sample surface, providing information about the topography and surface features. Tapping mode, on the other hand, operates with intermittent contact between the tip and the sample, which reduces the potential for damage to the sample surface. Non-contact mode involves oscillating the cantilever close to the surface without actual contact, allowing for sensitive measurements of forces or interactions[7,3].

In Fig. 2.4a the placement of cantilever during a contact mode AFM measurement, and resultant image of the measurement is shown. The placement of the cantilever in Atomic Force Microscopy (AFM) measurements is crucial and can significantly impact the quality and accuracy of the results. Here are a few key points highlighting the importance of cantilever placement:

Surface Interaction: The cantilever interacts directly with the surface being studied in AFM. The position and orientation of the cantilever determine the precise point of contact between the probe tip and the sample surface. Proper placement ensures that the desired region of interest is probed accurately.

Force Sensing: AFM measures the interaction forces between the cantilever and the sample surface. The placement of the cantilever affects the magnitude and distribution of these forces. Placing the cantilever in an appropriate location allows for the detection of subtle surface interactions, such as weak molecular forces or atomic-level features.

Topographical Mapping: One of the primary applications of AFM is high-resolution topographical mapping of surfaces. The accurate placement of the cantilever ensures that the probe tip scans the desired area, allowing for precise topographic measurements. Improper placement may result in missing or overlapping regions, leading to incomplete or distorted topographic data.

Tip-Sample Interaction: The interaction between the probe tip and the sample surface influences the imaging quality and measurement outcomes. Correct cantilever placement helps optimize the tip-sample interaction forces, minimizing artifacts such as tip-sample adhesion, lateral forces, or unwanted tip wear. This ensures accurate and reliable measurements.

Scan Speed and Stability: The placement of the cantilever affects the stability and scan speed of the AFM measurement. Placing the cantilever at an optimal position minimizes unwanted vibrations, drift, or mechanical noise during the scanning process, leading to smoother and more efficient measurements.

2.2.2.2. Scanning Electron Microscope (SEM)

Scanning Electron Microscopy (SEM) is a powerful imaging technique that allows for high-resolution imaging and analysis of surfaces at the micro- to nanoscale. It is widely used in various scientific disciplines, including materials science, nanotechnology, biology, geology, and forensic science.

SEM operates by scanning a focused electron beam across the surface of a sample. When the electron beam interacts with the sample, various signals are generated, including secondary electrons, backscattered electrons, and characteristic X-rays. These signals are detected and used to create detailed images and obtain information about the sample's topography, morphology, elemental composition, and crystal structure. The electron beam is generated by an electron gun and focused onto the sample surface using magnetic lenses. The beam is rastered across the sample in a scanning pattern, and the emitted signals are collected and processed to form an image. The resolution of SEM depends on several

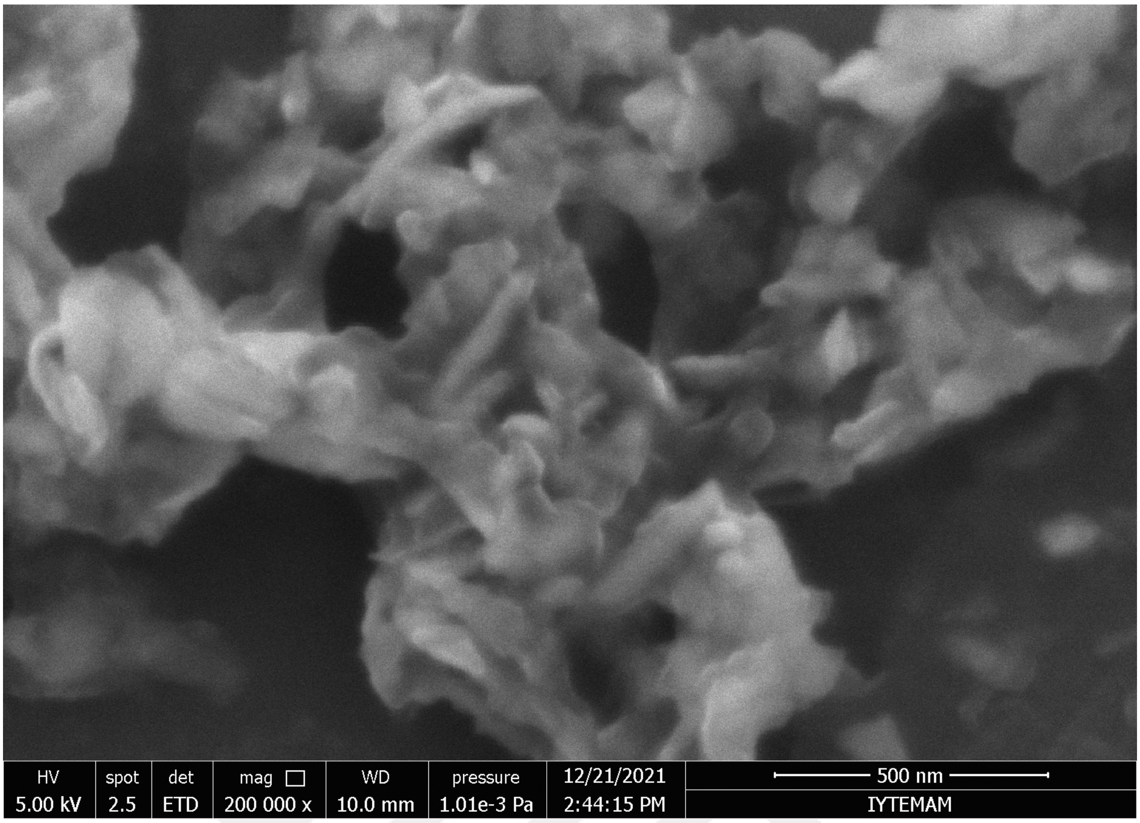

Figure 2.5. The captured Scanning Electron Microscopy (SEM) images of DDT-functionalized MoS_2 (DDT-MoS_2) samples on Si/SiO_2.

factors, including the electron beam energy, the size of the electron probe, and the detectors used to capture the emitted signals.

SEM provides high-resolution images with magnifications ranging from tens to hundreds of thousands of times. It offers a three-dimensional view of the sample surface, allowing for detailed examination of surface features, such as surface roughness, texture, and the size and shape of particles or structures. The technique also enables elemental analysis through energy-dispersive X-ray spectroscopy (EDS), where characteristic X-rays emitted by the sample are collected and used to identify and quantify the elements present[31,77].

2.2.2.3. Scanning Transmission Electron Microscope (STEM)

When the secondary electron (SE) detector in a scanning electron microscope (SEM) is replaced with a transmission electron (TE) detector, the SEM essentially transforms into a scanning transmission electron microscope (STEM).

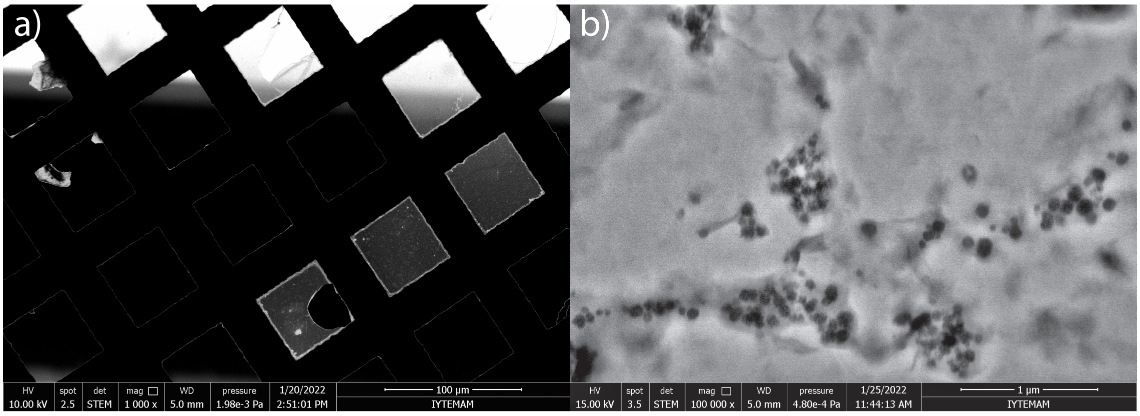

Figure 2.6. The captured Scanning Transmission Electron Microscopy (STEM) images of DDT-functionalized MoS_2 (DDT-MoS_2) samples on TEM grid. a) Apparent cage and net part of the TEM grid and b) zoomed bundles of DDT-MoS_2.

The primary difference between SEM and STEM lies in the detection and imaging mechanism. In a standard SEM, the SE detector captures the secondary electrons emitted from the sample's surface upon interaction with the primary electron beam. These emitted electrons provide information about the surface topography and composition.

On the other hand, in a STEM, a focused electron beam is transmitted through the sample rather than scanning the surface. The transmitted electrons pass through the sample and interact with its internal structure. A TE detector is positioned below the sample to capture the transmitted electrons that have passed through the sample[95].

By collecting the transmitted electrons, the STEM allows for high-resolution imaging of the sample's internal structure, providing detailed information about its composition, crystal structure, and other characteristics. This makes STEM particularly useful for studying thin sections, nanoparticles, and materials with complex internal structures.

In addition to imaging, STEM also enables other analytical techniques, such as electron energy-loss spectroscopy (EELS) and electron diffraction, which can provide elemental composition and crystallographic information, respectively. These capabilities make STEM a versatile tool for materials characterization and analysis at the nanoscale[74].

2.3. Theoretical Methodology

2.3.1. Density Functional Theory (DFT)

Density Functional Theory (DFT) is a computational method used to study the electronic structure and properties of molecules, materials, and solids. It is based on the concept that the ground-state electron density contains all the necessary information about the system. DFT provides a practical approach to solving the many-electron Schrödinger equation by focusing on the electron density rather than solving for the wavefunction of each electron explicitly. The electron density is determined self-consistently by minimizing the total energy of the system.

Hohenberg-Kohn Theorems: The Hohenberg-Kohn theorems are fundamental principles of DFT. They establish that the ground-state electron density uniquely determines the external potential and the total energy of the system[41].

1st theorem: The ground-state electron density uniquely determines the external potential. This theorem states that the electron density ρ(r) completely determines the system's external potential, V(r), except for an additive constant. In other words, if two different external potentials give rise to the same electron density, then they must be equivalent in terms of their effects on the system's properties.

$$\rho(r) \rightarrow V_{\text{ext}}(r)$$

2nd theorem: The ground-state energy is a functional of the electron density. This theorem states that the ground-state energy, E[ρ], can be expressed as a functional of the electron density. It implies that the total energy of the system is minimized when the exact electron density is used.

$$E[\rho] = F[\rho] + \int V_{\text{ext}}(r)\rho(r)\,dr$$

In these equations, $\rho(r)$ represents the electron density, $V_{\text{ext}}(r)$ is the external potential, $E[\rho]$ is the total energy functional, and $F[\rho]$ is the universal functional that accounts for the electron-electron interactions.

Kohn-Sham Equations: The Kohn-Sham equations are a set of equations derived from the Hohenberg-Kohn theorems. They introduce a set of auxiliary non-interacting electrons that produce the same electron density as the real interacting system[49].

The Kohn-Sham equations can be written as follows:

$$\left[-\frac{1}{2}\nabla^2 + V(r) + V_H(r) + V_{xc}(r)\right]\psi_i(r) = \varepsilon_i\psi_i(r)$$

In this equation, $\psi_i(r)$ represents the wavefunction of the i-th Kohn-Sham electron, ε_i is its corresponding energy eigenvalue, $V(r)$ is the external potential, $V_H(r)$ is the Hartree potential arising from the electron-electron repulsion, and $V_{xc}(r)$ is the exchange-correlation potential.

Hellman-Feynman Theorem: The Hellman-Feynman theorem is a fundamental concept in DFT. It states that the derivative of the total energy with respect to an external parameter is equal to the expectation value of the derivative of the Hamiltonian with respect to the same parameter. This theorem allows for the calculation of forces and related properties by considering the change in energy with respect to external perturbations. It forms the basis for techniques such as geometry optimization and molecular dynamics simulations[38].

$$\frac{dE}{d\lambda} = \langle\frac{d\hat{H}}{d\lambda}\rangle$$

In this equation, E represents the total energy of the system, λ is a parameter (e.g., nuclear coordinate or external field strength), $\hat{H}$ is the Hamiltonian operator, and $\langle\rangle$ denotes the expectation value.

2.3.1.1. Algorithm & Method of a DFT Calculation

It has been an important task for experimental scientists to understand how the DFT tool, which is created by utilizing the theorems described in the previous section and can describe quantum systems very effectively and make the energetic analysis impressively accurate, works and how it operates behind the codes. As it is stated before, DFT is a computational tool that plays a pivotal role in understanding and predicting the properties of atoms, molecules, and solids. In this section, we delve into a detailed explanation of the DFT algorithm, focusing on its fundamental principles and the concept of self-consistency. Additionally, we provide illustrative figures to help visualize the DFT algorithm and the ion calculative process.

At its core, DFT seeks to solve the many-body Schrödinger equation by describing the electronic system in terms of the electron density rather than the wavefunction. This approach reduces the computational complexity significantly, making it feasible to study systems of practical interest. The key idea behind DFT lies in the Hohenberg-Kohn

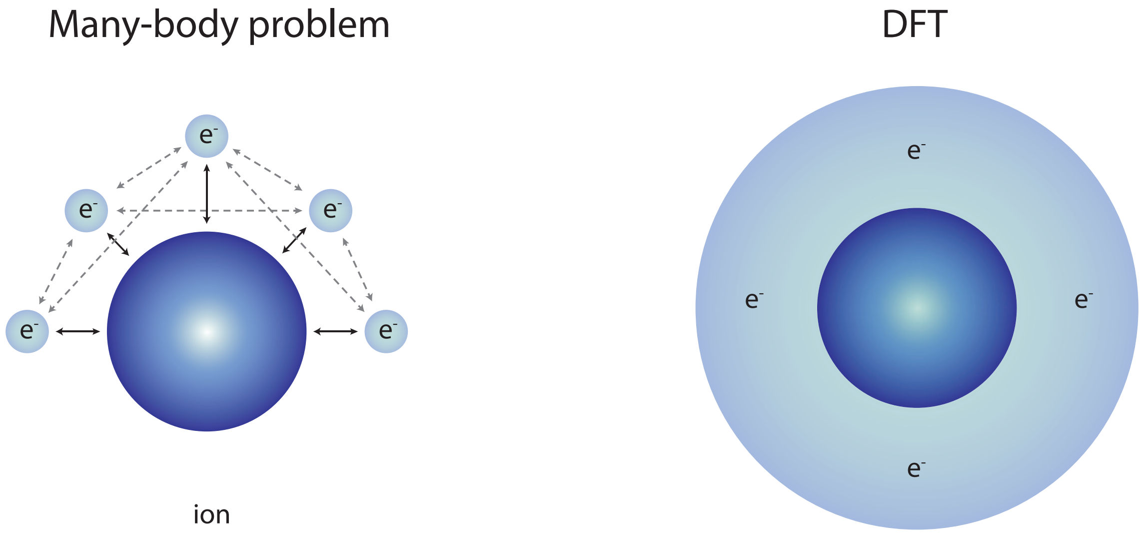

Figure 2.7. llustration of the many-body interaction problem being addressed by Density Functional Theory (DFT). DFT tackles the complex interactions among electrons in a system by mapping it onto an effective single-particle problem governed by the exchange-correlation functional, enabling the calculation of properties such as electronic structure and energies.

theorems, which state that the ground-state electronic density uniquely determines the external potential and the total energy of a system.

The DFT algorithm begins by specifying an initial guess for the electron density. This guess is typically based on a simple model or the superposition of atomic densities. The next step involves solving the Kohn-Sham equations, which are a set of auxiliary single-particle Schrödinger-like equations. These equations introduce a set of fictitious non-interacting electrons moving in a self-consistent effective potential.

To establish self-consistency, the algorithm iteratively improves the electron density until convergence is achieved. In each iteration, the current electron density is used to calculate the effective potential, which is then fed back into the Kohn-Sham equations. This process is repeated until the electron density converges, indicating that the total energy of the system has reached a minimum and the self-consistency has been achieved.

Fig.2.7 illustrates the general flow of the DFT algorithm. It shows the iterative steps involved in obtaining the self-consistent electron density. Initially, the algorithm starts with an initial guess for the density. The Kohn-Sham equations are solved, yielding the new electron density. This density is compared to the previous iteration, and if the convergence criterion is not met, the process iterates. Once convergence is achieved, the algorithm terminates, and the self-consistent electron density is obtained.

To further clarify the DFT ion calculative process, Fig.2.8 presents a schematic representation. It depicts the interaction between the ion and the electron cloud. The ion, represented by a plus sign (+), generates an electrostatic potential that influences the electron density distribution (ρ). Through the self-consistency loop, the electron density adjusts in response to the ion's potential until an equilibrium state is reached. This equilibrium represents the ground-state configuration of the system.

In conclusion, the DFT algorithm provides a powerful framework for studying the electronic structure and properties of diverse systems. By emphasizing the concept of self-consistency, DFT enables accurate calculations of ground-state properties. The iterative nature of the algorithm and the continuous adjustment of the electron density ensure convergence and reliable results. Figures 1 and 2 help visualize the DFT algorithm and the ion calculative process, providing a clearer understanding of the underlying concepts and procedures involved in DFT calculations.

The exchange-correlation functional is an essential component of DFT. Various exchange-correlation functionals exist, ranging from local density approximation (LDA) to generalized gradient approximation (GGA) and more advanced hybrid functionals. The choice of functional depends on the specific system and properties of interest[75,49].

2.3.2. Computational Parameters

This section provides an overview of the methodology used in the thesis, focusing on the Density Functional Theory (DFT) approach. It discusses the computational parameters employed for the calculations, highlighting their significance in obtaining accurate and reliable results. The section aims to establish a foundation for the subsequent analyses and interpretations presented in the thesis.

In Chapter 3, for the accurate representation of experimental data, first-principle density functional theory (DFT) calculations were performed with Vienna ab-initio Simulation Package using projector augmented wave (PAW) potentials[50,51,8]. The generalized gradient approximation (GGA) of Perdew-Burke-Ernzerhof (PBE) was used for the exchange-correlation functional[76]. The van der Waals interactions were included by utilizing the DFT-D2 method of Grimme[34]. The geometric relaxation of atoms set to come to a halt when pressures in all directions were less than 1 kB. Brillouin zone sampling was performed with automatic k-point meshes. For the hexagonal unit cell, a grid of $3 \times 3 \times 1$ was used, and the k-point grid scales with the supercell dimensions. To avoid interaction between vicinal monolayers, a vacuum spacing of at least 10 Å was taken. The total energy difference of 10^{-5} eV between the sequenced ionic steps was taken as the convergence criteria. For the density of states (DOS) calculations, a Gaussian smearing width of 0.05 eV was used.

In Chapter 4, interaction of the target gas methanol and differently synthesized graphene sensors were modeled using specified methodology. Vienna Ab initio Simulation Package (VASP) was used for the determination of optimal crystal structures and resulting electronic properties of the interactions of graphene and methanol species. The projector augmented wave (PAW) method was utilized in order to describe the pseudo-potentials of carbon atoms[50,51,8]. The exchange-correlation functional was treated by the generalized gradient approximation (GGA) as parametrized within the Perdew Burke-Ernzerhof (PBE) form[76]. The DFT-D2 method was used to implement the van der Waals (vdW) corrections[34]. The plane-wave functions were expanded up to a 500 eV of kinetic energy cut-off while the criterion for total energy convergence was taken to be 10^{-6} eV. 15 Å of vacuum spacing was introduced in order to prevent interactions between repeating structures along the out-of-plane direction. The total system consists of a $5\times5\times1$ graphene supercell with a single molecule adsorbed to graphene species. During the ionic relaxations, the Brillouin Zone (BZ) was sampled using $3\times3\times1$ k-points.

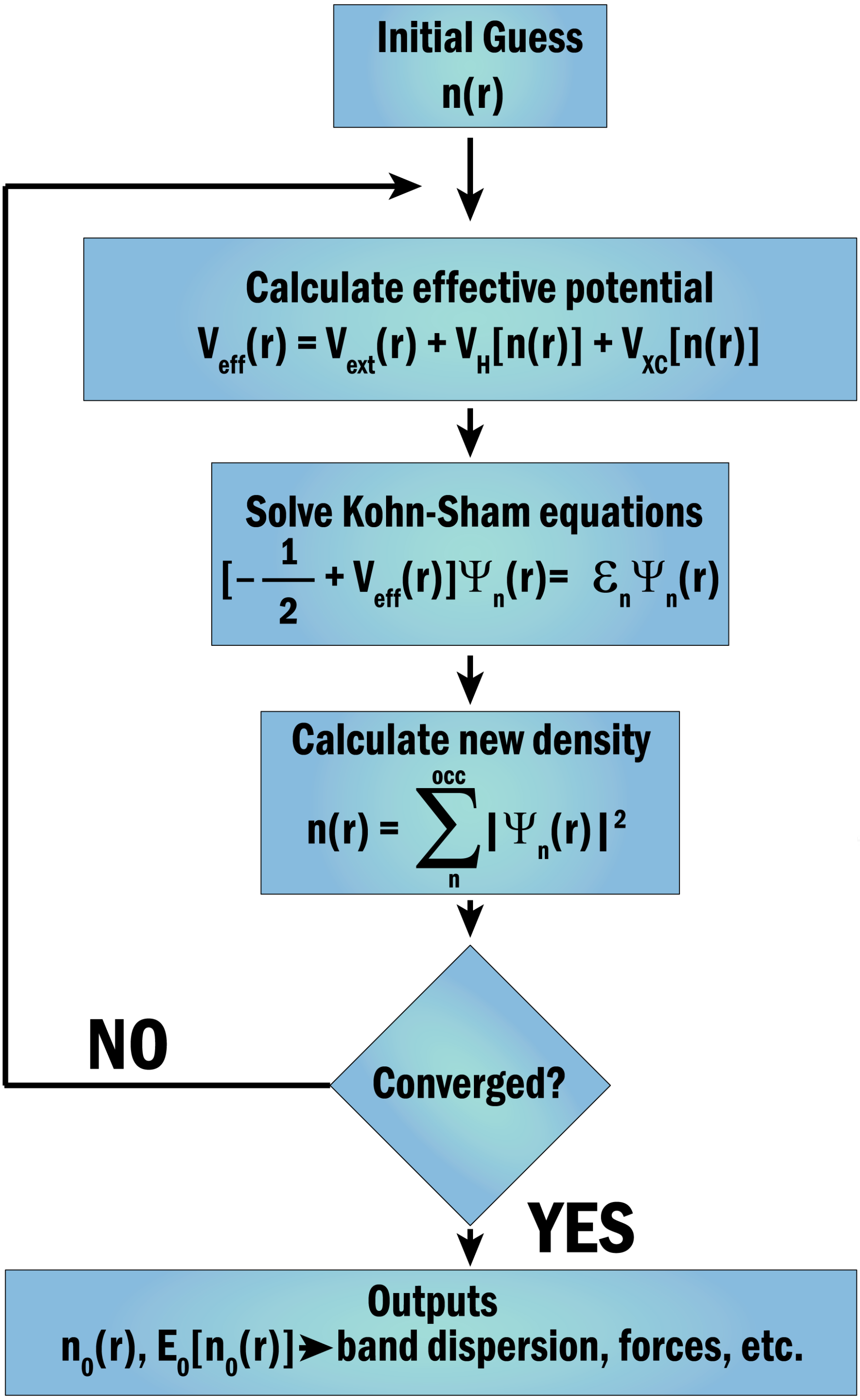

Figure 2.8. Schematic representation of the DFT self-consistency algorithm. The iterative process involves the calculation of electron densities, exchange-correlation potentials, and total energies, which are used to update the electron density until self-consistency is reached.

CHAPTER 3

EXPERIMENTAL AND THEORETICAL INVESTIGATION OF SYNTHESIS AND PROPERTIES OF DODECANETHIOL FUNCTIONALIZED MOS$_2$

Graphene, a two-dimensional (2D) and atom-thick carbon material has received great interest owing to its ultrahigh carrier mobility, thermal conductivity and mechanical strength[27,72]. As a member of 2D materials family, a group of layered materials such as transition metal dichalcogenides (TMD) has been studied widely due to their interesting thickness-dependent optical, electrical and mechanical characteristics[58]. In the past decade, TMDs such as molybdenum (IV) disulfide are used extensively in the form of nanostructures[66], van der Waals heterostructures[87], nanocomposites[82], compositional heterojunctions[80], 3D foams[104] and functionalized TMD nanosheets[61,10,35].

In its base form, the bulk and non-luminescent MoS$_2$, gain access to its luminescent properties upon exfoliation[23,44]. The bulk crystal structure of MoS$_2$ consists of weakly interacted 6.5 Å thick MoS$_2$ layers with a van der Waals (vdW) gap, which allows multi-layered structures like MoS$_2$ to be exfoliated. In general opinion, the MoS$_2$ layers are accepted as chemically inert species, specifically, the basal sites of the vdW stacked layered composition of 2H-MoS$_2$[13]. It seems logical that the broken bonds at the MoS$_2$ layer edges would increase reactivity[14], and it has been demonstrated that the edge sites of 2H-MoS$_2$ exhibit different electrical characteristics than those of the pristine basal plane[43].

To further expand the utilization of MoS$_2$ and to amplify the characteristics of interest towards desired applications, covalent and non-covalent basal and edge-plane functionalization have been utilized over the years. In doing so, a variety of functionalized-MoS$_2$ have been used throughout the last decade for the applications in solar cells[5], catalysis[93], sensors[65], photodynamic/photothermal therapy[19,22], biosensors[94], tissue engineering[81], and cell imaging[79].

While functionalization provides a wide range of applications that are suitable for understanding the nature of absorption in different regions of the electromagnetic spectrum, it especially opens a door to many variations of diode and photoresponsive sensor device designs and structures[52]. In the field of advanced sensors, sensors with low detection limits are often nanoparticle-sensitized 2D materials and atomic-thick 2D materials have continued to attract great attention for specific parts of infrastructures of sensor devices. However, the enhancement of optical, electrical and thermal properties of MoS_2 continues at full speed today. The functionalization of MoS_2 with organic molecules bearing thiol functional groups during exfoliation has been studied as a whole new area of thiol-conjugated transition-metal disulfides. However, in the case of 1-Dodecanethiol (DDT) functionalization, there is an insufficient number of studies that have been reported previously. For instance, Ahmad et al.[1] propose an optimized method that involves oleylamine (OLA) and DDT-assisted exfoliation procedures for the thinning of bulk MoS_2, which is utilized in a 2D/0D hybrid of MoS_2/$CuInS_2$ quantum dots. Park et al.[73] report a facile method for enhancement of chemically exfoliated 1T-MoS_2, by annealing and simultaneously treating with DDT molecules in the presence of, therefore exchanging Mo-O with Mo-S bonds. In the aforementioned previous studies examining the functionality of MoS_2 with DDT, the unintentionally generated quantum dots of the sonication-assisting solvent were not mentioned. In this study, both the interaction of quantum dots with MoS_2 and the role of self-assembly monolayer formed of DDTs were investigated.

In this study, motivated by the recent cost-effective synthesis of low-dimensional TMDs, we propose a mechanism of functionalization of MoS_2 via the DDT molecule. DLS size analysis showed that there is a formation of heterostructure in the system when DDT is involved. AFM and STEM analysis gave insight into the orientation of the heterostructure formed, which is residual GQDs on MoS_2 particles. A thorough analysis based on DFT simulations, for bare and functionalized heterostructures of MoS_2, is in agreement with the proposed infrastructure of the heterostructure.

3.1. Examination of Bare Exfoliated MoS_2 in NMP

Synthesis of DDT-MoS_2 Bulk Suspension: Suspensions with a concentration of 100 mg/mL were prepared by mixing 100 mg of MoS_2 bulk powder (Sigma-Aldrich, 98%) with 1 mL of 1-Dodecanethiol (Sigma-Aldrich, 98%) and stirring the suspension for 3 hours at 70 degrees Celsius, then keeping the flask stirred for 20 hours at room temperature afterward, at ambient.

Synthesis of DDT-MoS_2 Exfoliated Suspension: After the preparation of the DDT-MoS_2 precursor, the suspension is put in a beaker and mixed with 9 ml of NMP. This DDT-NMP-MoS_2 mixture is sonicated with the probe-tip sonication method. The sonication procedure consists of a 20-minute sonication of the sample with a pulse of 7 s on and 5 s off and a power of 130 W. During the sonication, to avoid overheating of both

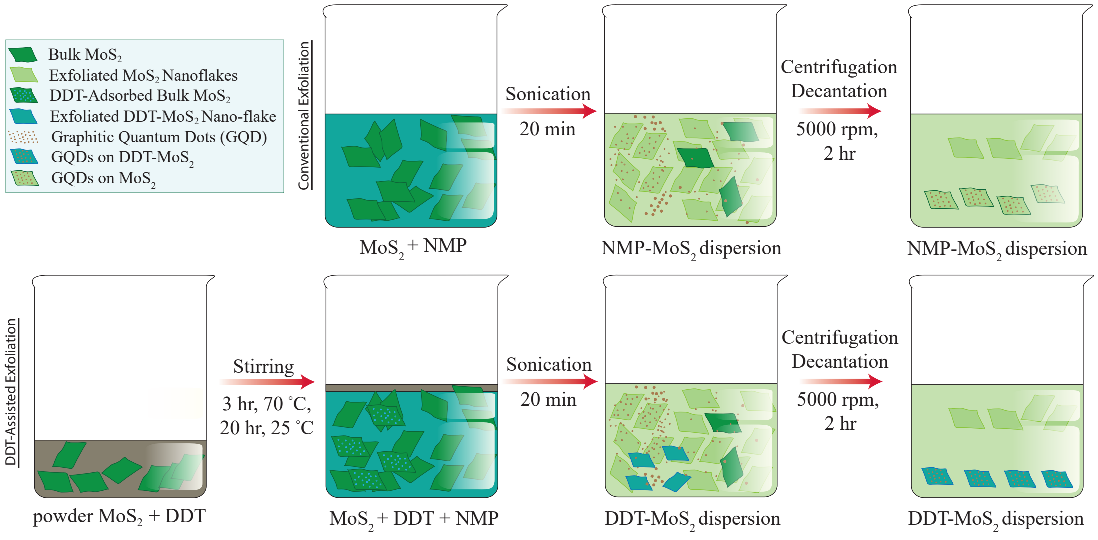

Figure 3.1. A detailed synthesis route for the conventional liquid phase exfoliation and DDT-assisted exfoliation of MoS_2.

the dispersion and tip-probe sonicator and stabilize the sample at the desired temperatures, an ice-bath is employed for every 10 minutes of sonication. (Nanolinker, NL650) The dispersion acquired from sonications was centrifuged (Nuve, NF1215) at 5000 rpm for 2 hours to discard the bulk MoS_2 from separated MoS_2 layers. Afterward, the suspension is purified by adding excess acetone and discarding the organic phase. The summary and schematic of the procedure are given in Fig.3.1.

Cleaning of SiO_2/Si: Commercial SiO_2(300 nm)/Si substrates were first cleaned via Piranha solution and rested in DI water. Then, bath-sonication was employed onto SiO_2/Si substrates for 10 minutes in acetone, ethanol (EtOH), and isopropanol (IPA) for the removal of the solvent residues, respectively, and the substrates were dried via N_2 purging. Thereafter, the exfoliated DDT-MoS_2, NMP-MoS_2 and sNMP suspensions were drop-cast onto the sterilized SiO_2/Si substrates and put in a vacuum oven to remove solvent residues.

Characterization: Absorbance and photoluminescence (PL) spectra were acquired using the HORIBA Duetta with a Xenon light source with a power of 75 W. Before the measurements, MoS_2 dispersions in IPA and NMP were held in a quartz cell during optical analysis, and the background correction was performed by placing a quartz cell filled with NMP. Raman Spectroscopy analyses were conducted with a Raman Microscope (HORIBA, XploRA PLUS) under ambient conditions, with an operating wavelength of 785 nm and a spectral resolution of 1 cm^{-1}. The calibration was performed with the Si peak at 520 cm^{-1}. Bright field Scanning Transmission Electron Microscope (STEM) images were taken on Si/SiO_2 substrates. STEM images were taken by implementing a transmission detector in

FEI, QUANTA 250 FEG with an accelerating voltage of 15 kV. Atomic Force Microscopy (AFM) images were taken on Si/SiO_2 substrates (Bruker-MMSPM Nanoscope 8). Dynamic Light Scattering measurements are done in NMP solvent (Malvern Panalytical, ZetaSizer).

While there are rapid developments in the synthesis of nanoscale materials, a reliable characterization of the obtained products is also of importance. Considering this need, vibrational spectroscopy stands out as a simple and effective method. Therefore, we first investigate the Raman characteristics of the exfoliated MoS_2 samples.

The Raman spectrum shown in Fig.3.2(a) can be divided into two main regions: (i) MoS_2 regions extend between 370 and 460 cm^{-1} and (ii) the by-product region between 1250 and 1650 cm^{-1}. In the MoS_2 region, there are three prominent Raman active phonon branches. While the $E^1{}_{2g}$ peak at 378 cm^{-1} originates from the in-plane out-of-phase vibration of Mo and S atoms, A_{1g} at 403 cm^{-1} is due to the out-of-plane vibration of S atoms. In addition, 2LA peak located around 450 cm^{-1} emerges as a result of the second-order Raman process involving the longitudinal acoustic phonon at the M point of the Brillouin Zone[68]. The Raman spectrum reveals that, differing from the $E^1{}_{2g}$ and the A_{1g} peaks, the 2LA branch has an anti-symmetric shape nature due to its multi-phononic nature.

Moreover, the high-frequency phonons appearing in the Raman spectrum of MoS_2 crystals obtained by chemical exfoliation are also noteworthy. It is known that during the probe sonication process, the probe tip heats its surroundings to extreme temperatures by generating alternating series of low and high-pressure waves in the solvent[20]. Therefore, one can expect NMP solvent to undergo dramatic structural modifications such as polymerization and isomerization during the solvothermal synthesis processes[102]. Our calculations reveal that, as shown in Fig.3.2(b), NMP molecules in a vacuum interact with one another via hydrogen-type bonds with a binding energy of 70 meV. In addition, the hydration of NMP significantly enhances intermolecular interactions to the order of 600 meV. Moreover, the binding energy of each NMP on the MoS_2 surface is calculated to be 770 meV without any charge transfer. Despite the fact that the formation of strong covalent bonds between NMP molecules or the host MoS_2 lattice is not expected, clusterization of NMPs on the basal plane of MoS_2 is likely to happen. In addition, MD calculations (performed for temperatures from 0 to 5000 K in 5 ps) show that bond dissociation in NMP molecules and the formation of various carbon-based clusters take place starting from 4250 K. Therefore, it can be deduced that the carbon-based particles formed by carbonization of NMP molecules are GQDs and the peaks located at the vicinity of 1350 cm^{-1}, 1600 cm^{-1} and 2635 cm^{-1} are attributed to D, G and 2D peaks, respectively, of graphitic materials. The intensity ratio of D/G hints to the character of a defective graphitic material. The high frequency Raman lines exhibit an approximate ratio of 1, which is evident in previous studies that this D/G ratio refers to a GQD structure with the chemical nature of a graphene-oxide[2].

For further characterization of the obtained composite material, absorption and photoluminescence measurements are also performed. Fig.3.2(c) shows that the absorption peak[69] of MoS_2 exfoliated in NMP solvent is at 2.45 eV. While the absorption edge correlates with the peaks between 550 and 700 nm in the visible region in the photoluminescence spectrum (Fig.3.2(d)), the shifting behavior of peaks according to the energy of the excitation laser confirms that the photoluminescent particles are in the form of quantum dots. However, it is clear that the source of the PL peaks around 1000 nm is the GQDs, rather than MoS_2 crystals, that emerge during sonication. Moreover, recently, both the theoretical investigation on the size and shape-dependent luminescent properties, and synthesis-application of NIR-luminescent GQDs are studied and discussed in detail in previous studies[83].

The 2D AFM topographical image shown in Fig.3.2(e) reveals that the sonication of MoS_2 yields agglomerated islands of particles. The height profiles of the particles along the marked sections demonstrate a height of 10-40 nm. The AFM size distribution data in Fig.3.2(f) shows that the exfoliated NMP-MoS_2 particles vary in the range of 50-150 nm as well. When the AFM image is examined closely, it is seen that the individual particles have grain boundaries, and this implies the particles' formation happens through agglomeration of smaller particles. In the STEM image shown in Fig.3.2(g), the smaller GQD particles appear to be scattered around MoS_2 nanoflakes. According to the DLS analysis in Fig.3.2(h), the 1-2 nm particles correlated in the STEM image are the result of bare NMP sonication, which is related to the GQD formation. Moreover, in the aqueous phase, NMP-MoS_2 is dispersed rather than agglomerated. Therefore, the sizes of NMP-MoS_2 seem to be much lower (around 10 nm) than in the AFM results.

3.2. Functionalization by Dodecanethiol

Understanding how 2D crystalline materials can be functionalized and what properties they can acquire when they are functionalized is important in terms of finding more uses in technological applications. In this context, functionalization of MoS_2 crystals by means of thiol-based organic molecules such as DDT stands out as a cheap and effective method due to its sulfurous structure[59,62].

A reliable prediction of how MoS_2 crystals interact with DDT molecules during the experimental functionalization process can be achieved with DFT-based calculations. As shown in Fig.3.3(a), the binding energy of DDT on defect-free MoS_2 surface is 0.70 eV from the sulfur side and 0.68 eV from methyl side of the molecule. Bader analysis shows that DDT molecules tend to form strong bonds without charge transfer, regardless of which ends they approach the MoS_2 crystal. In addition, the occurrence of structural defects in the experimental synthesis and transfer process is inevitable, and the most prominent among these are sulfur vacancies[57]. For the S-vacant state, the binding energy of the DDT molecules from the methyl end increases slightly to 0.69 eV. However, the interaction energies of the sulfuric ends of DDT molecules on S-vacant regions of MoS_2 increase dramatically up to 0.95 eV. It seems that even if there are structural defects that occur in the MoS_2 crystal during the sonication with NMP, the defect-induced electronic and optical instability can be eliminated by the non-covalent DDT-functionalization. AFM and DLS analyses demonstrate that MoS_2 crystals synthesized by exfoliation method mostly consist of flakes ranging in size 50-100 nm and also reveal that in addition to basal plane, interaction of DDT molecules with edges must also be taken into account. As shown in Fig.3.3(a), the interactions of DDT molecules with the zigzag and armchair edges of MoS_2 were investigated. It is seen that each DDT interacts with the zigzag edge with a binding energy of 0.91 eV (2.67 eV) from its methyl (sulfur) side. Similarly, for armchair edges of MoS_2 flakes binding energy per DDT molecule is calculated to be 0.82 eV (2.31 eV) from its methyl (sulfur) side. Apparently, it is reasonable to assume that while the basal plane of MoS_2 is functionalized through strong S-S interactions, the edges are theoretically expected to be terminated via partly covalent-ionic binding between the Mo atom of the edge and the S atom of the DDT. The AFM analysis of DDT-functionalized MoS_2 is shown in Fig.3.3(b-c). What appears at first glance in the AFM image is the relatively large yellow spots appearing on large fragments. Particle size analysis clearly reveals that both GQDs and MoS_2 flake sizes increase in the presence of DDT. In addition, STEM analysis presented in Fig.3.3(c-d) also shows that the synthesized DDT-MoS_2 bundles appear as large flakes. Based on the DLS data in Fig.3.3(e), quantum dots of 50-100 nm are adsorbed on MoS_2 flakes with an average length of 275 nm (Fig.3.2(h) and Fig.3.3(e)). Here it is seen that the presence of DDTs provides a strong interaction of both ends of the DDT molecules and the MoS_2 edges results in larger MoS_2 fragments. This strong interaction can be further hinted by changed zeta potential values of systems. While NMP-MoS_2 has a zeta potential of 4 mV, DDT-functionalized MoS_2 has a zeta potential of -7 mV. Therefore, our experimental results show that the surface charge of different samples are changed negligibly.

Additionally, since the emergence of GQDs in the sonication-based exfoliation process is inevitable, it is of importance to understand how they interact with DDT molecules. As shown in Fig.3.4, the binding energy of DDT with the basal plane of GQD is 1.28 eV from its sulfur side and 1.32 eV from methyl side. It is also seen that DDT molecules strongly interact with the edges of GQDs with a binding energy of 1.23 (1.25) eV from their methyl (sulfur) side. Therefore, although the DDT-GQD interactions are energetically favorable, there is no absolute distinction between the different sites of adsorption of DDT onto the GQDs. Moreover, to examine the formation of micelle-like structures and the effect of moisture DDT-DDT and DDT-H_2O interactions are also investigated theoretically. DDT-DDT interaction is calculated to be 0.18 eV (0.39 eV) for parallel (anti-parallel) orientation of DDT molecules. Furthermore, while H_2O molecules weakly bind to the hydrogenated sites of the DDT molecule bonding is quite large (0.23 eV) at the sulfur side of the DDT molecule. It is clear that the surfaces of GQDs are tightly surrounded by DDTs during the functionalization process. It can be inferred that the GQD-DDT clusters are able to form micelle-like structures by strongly interacting with water molecules from their sulfide ends.

The Raman measurement showing the vibrational spectra of DDT-functionalized MoS_2s is presented in the Fig.3.5. First of all, it is seen that the increase in the number of DDT molecules leads to hardening in the prominent phonon modes ($E^1{}_{2g}$ and A_{1g}) of MoS_2. While dispersed MoS_2 via NMP exhibit Raman lines at 378 and 403 cm^{-1}, respectively, the peaks of MoS_2 dispersed in DDT-NMP 1:9 (DDT-NMP 5:5) emerge at 380 cm^{-1} (383) and 405 (408) cm^{-1}. Such phonon hardening, which occurs as a result of strong interaction of DDT molecules with the MoS_2 surfaces, is clearly associated with the reduction in the crystal lattice[15]. Another finding in the Raman spectrum of DDT-MoS_2 is that the intensity of the edge and defect-induced 2LA phonon mode decreased dramatically with the increasing amount of DDT in the medium. Apparently, defect healing and edge termination of DDT-MoS_2 particles can be monitored via 2LA phonon branch. In addition, vibrational characteristics of GQDs show that while DDT functionalization leads to a remarkable increase in phonon intensities, negligible shift in their phonon frequencies is observed. Apparently, the vibrational characteristics of both MoS_2s and GQDs change dramatically with functionalization.

For optical characterization of the functionalized crystal structures, the photoluminescence spectra of NMP-MoS_2, DDT-MoS_2 and GQDs are also given in Fig.3.6(a). It is seen that the intensity of MoS_2 originated PL peaks is significantly enhanced due to the DDT functionalization. Similarly, the PL intensities of GQDs stimulated in the high wavelength region are increased by up to 60-fold with the effect of DDT functionalization. Here, the peak positions displaying dependence on the excitation wavelength indicate that the DDT-covered luminescent particles are still in the form of quantum dots. Here, the DDT-induced increase in the optical visibility of functionalized products requires explanation. As schematized in the Fig.3.6(b), the surfaces of MoS_2 and GQD are coated with DDT, resulting in spatial separation between these two material groups. Therefore a reasonable theoretical explanation of enhanced PL intensity can be obtained by employing Anderson's rule used for the construction of energy band diagrams of the heterojunctions. In the absence of DDTs, the interface obtained by the combination of GQDs and MoS_2 materials forms a type-II heterojunction. Upon excitation, the lowest possible energy state (LUMO) for electrons in this heterostructure originates from MoS_2, while the highest energy level (HOMO) where holes can be found originates from GQDs. Therefore, the PL intensity obtained from excitations in a such heterojunction is low. However, it is seen that the HOMO states of DDT molecules have lower energy than the HOMO (VBM) states of GQDs (MoS_2) and its LUMO state lies at a higher energy level than the band edge of GQDs and MoS_2. Therefore, it can be concluded that the binary structures of GQDs, MoS_2 dots and DDT are type-I heterostructures and the PL intensity is enhanced in these structures where excitation and recombination processes occur on the same type of material.

In this work, one-pot synthesis of dodecanethiol (DDT) functionalized MoS_2 was performed, and obtained heterostructures were further investigated in terms of their morphological, optical and vibrational properties by both experimental and theoretical tools. For the purpose of performed functionalization, DDT treatment was incorporated into the traditional NMP-exfoliation process. It was shown that the process yields strong binding of DDT to the basal plane and edges of MoS_2, as corroborated by the theoretical binding-energy calculations. While the damped 2LA phonon modes were attributed to the DDT-functionalization, we found that the photoluminescence enhancement is caused by the formation of type-I heterostructure with the DDT encapsulation.

3.3. Enhancement of Sensor Response via DDT-Functionalization

The optical properties of MoS_2 enhanced through functionalization have been discussed in previous sections. Since there is a direct correlation between optical and electronic properties, this thesis also encompasses the investigation of utilizing functionalized

MoS_2 flakes in the fabrication of gas sensor devices and exploring the variations in their responses to volatile organic compounds (VOCs). By incorporating functionalized MoS_2 flakes, we can not only leverage their optical properties to understand their responses to VOCs but also gain insights into the role of their electronic properties. This research aims to contribute to the understanding of the relationship between functionalization, optical and electronic properties of MoS_2, and its applicability in gas sensing technology.

In the experimental methodology section, the exfoliation of MoS_2 flakes was performed using the LPE method, while DDT-MoS_2 samples were synthesized through the functionalization process described earlier in this chapter. To enhance the adhesion of the flakes, a mixture of MoS_2 and pure graphite powder was prepared and transformed into an ink solution. This ink solution was then carefully applied onto glass substrates. Two different types of samples, NMP-MoS_2 and DDT-MoS_2, were prepared and coated onto glass substrates using the drop-casting technique. The coatings were carefully placed between two Au/Cr electrodes with precise dimensions of 80 nm thickness and 300 microns separation. To evaluate the sensor response, two independent measurements were conducted on the prepared samples, providing valuable data for further analysis, as illustrated in Fig.3.7. This experimental approach enables a comprehensive investigation of the sensor performance and the influence of different substrate materials on the gas sensing properties of MoS_2 flakes. In the Fig.3.7a), the sensor response response of NMP-MoS_2 is shown which consists of four areas. In the first area, the surface was purged with N_2, resulting in a significant 90% increase in current, indicating a remarkable recovery. Moving to the second area, the introduction of acetone did not yield any response on the sensing surface. Similarly, in the third area, ethanol also did not elicit a response on the sensing surface. However, in the fourth area, when methanol was introduced, a moderate response of approximately 15% was observed on the sensing surface. These observations highlight the varying sensitivities of the sensor to different substances, with N_2 purging proving highly effective in restoring the current levels in the first area.

In the Fig.3.7a), the sensor response response of DDT-MoS_2 is shown which consists of eight areas. In the first area, the surface was purged with N_2, resulting in a 30% increase in current, indicating a 30% recovery. In the second area, while venting, the cap of the flask popped off, exposing it to the ambient atmosphere, leading to a slight decrease of 8% in current. Moving to the third area, the presence of acetone on the sensing surface yielded a 30% response. The fourth area involved N_2 purging, which resulted in a 45% recovery in current. In the fifth area, ethanol on the sensing surface produced a 45% response. N_2 purging was performed again in the sixth area, leading to a 60% recovery in current. The seventh area involved the presence of methanol on the sensing surface, which resulted in a 60% response. N_2 purging in the eighth area led to a significant recovery of 90% in current.

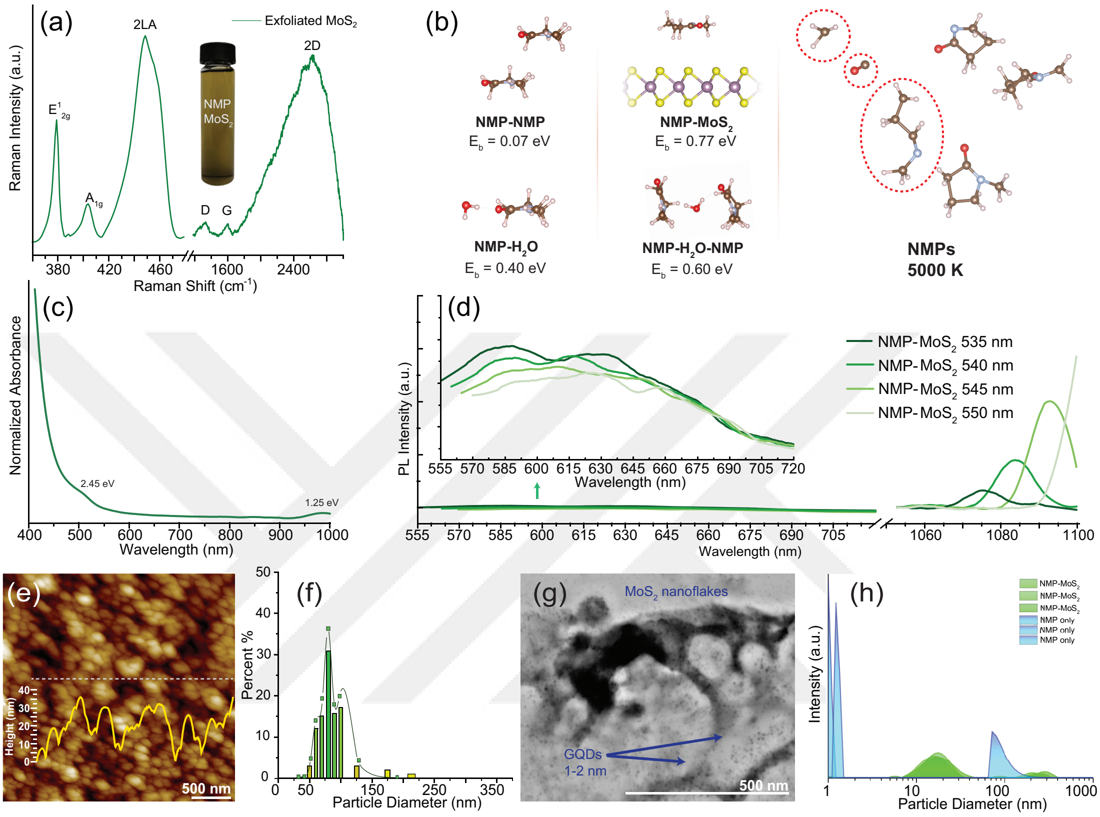

Figure 3.2. (a) Raman spectrum of dry NMP-MoS_2 on Si/SiO_2 substrate, excited with the laser of 785 nm. (b) Binding energies of NMP, in different molecule pairs and Molecular Dynamics (MD) simulation snapshot at 5000 K of liquid NMP solvent on Vienna ab-initio Simulation Package (VASP) software. (c) UV-Vis absorption spectrum of the as-exfoliated liquid NMP-MoS_2 sample. (d) Photoluminescence spectrum of the liquid NMP-MoS_2 sample, excited with 535, 540, 545 and 550 nm excitation wavelengths. (e) AFM image and and cross section height profile and (f) AFM particle size distribution of NMP-MoS_2 on Si/SiO_2 substrates. (g) Bright-field STEM images of exfoliated NMP-MoS_2 samples. (h) DLS size distributions of NMP-MoS_2 and sonicated bare NMP samples.

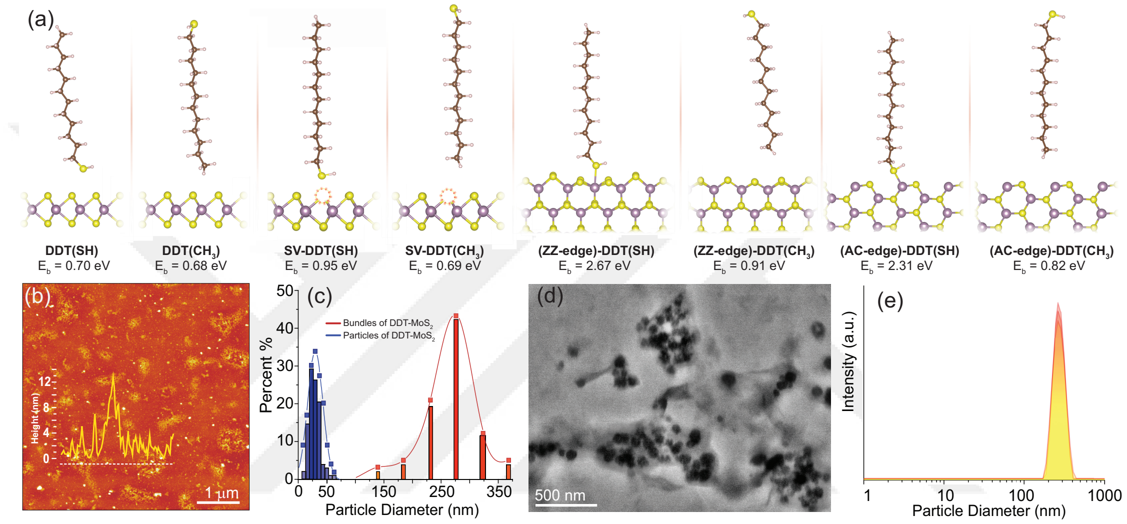

Figure 3.3. (a) Computed theoretical binding energy values of the interactions of pristine MoS_2-DDT, sulfur-vacant (SV) MoS_2-DDT, zigzag (ZZ) and armchair (AC) edge sites of MoS_2 with the both ends of the DDT molecule. (b) AFM image and and cross section height profile and (c) AFM particle size distribution of DDT-MoS_2 bundles (red) and particles (blue) on Si/SiO_2 substrates. Measured bundles in AFM size distribution are marked with black dashed lines in the AFM image. (g) Bright-field STEM images of exfoliated DDT-MoS_2 samples. (e) DLS size distribution of DDT-MoS_2 samples.

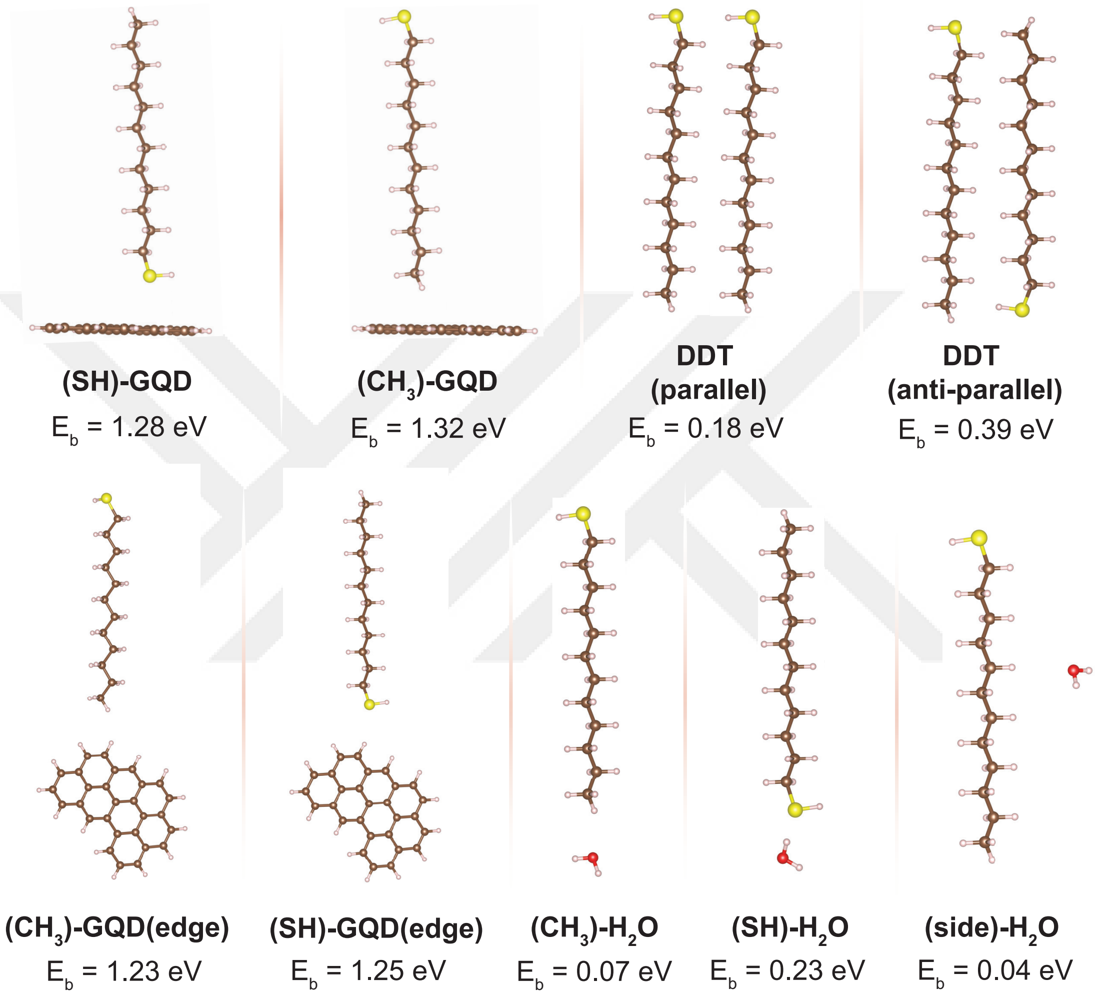

(SH)-GQD E_b = 1.28 eV

(CH$_3$)-GQD E_b = 1.32 eV

DDT (parallel) E_b = 0.18 eV

DDT (anti-parallel) E_b = 0.39 eV

(CH$_3$)-GQD(edge) E_b = 1.23 eV

(SH)-GQD(edge) E_b = 1.25 eV

(CH$_3$)-H$_2$O E_b = 0.07 eV

(SH)-H$_2$O E_b = 0.23 eV

(side)-H$_2$O E_b = 0.04 eV

Figure 3.4. Calculated binding energy values of the interactions of GQD-DDT(SH), GQD-DDT(CH$_3$), DDT parallel and anti-parallel, GQD(edge)-DDT(CH$_3$), GQD(edge)-DDT(SH), DDT(CH$_3$)-H$_2$O, DDT(SH)-H$_2$O and DDT(side)-H$_2$O coordinations of active molecules in experimental media. Values of interaction energies are calculated in the order of GGA.

Table 3.1. A data sheet to identify the fashion of complex formation (the binding energies of DDT to GQDs and H_2O by the thiol and methyl terminal sites of the molecule.) and the binding of the DDT on different sites of MoS_2 layers. Possible net magnetic moments μ_{net} are given in Bohr magneton. Charge transfer ρ is the amount of electron transfer between the components of the related system.

Interaction	**E_b(eV)**	$\mu(\mu_B)$	ρ**(e)**
MoS_2-NMP	0.77	0.0	0.01
NMP-NMP	0.07	0.0	0.00
NMP-H_2O	0.40	0.0	0.03
NMP-H_2O-NMP	0.60	0.0	0.02
Bare MoS_2-DDT(SH)	0.70	0.0	0.04
Bare MoS_2-DDT(CH_3)	0.68	0.0	0.00
SV-MoS_2-DDT(SH)	0.95	0.0	0.02
SV-MoS_2DDT(CH_3)	0.69	0.0	0.00
ZZ-Edge MoS_2-DDT(SH)	2.67	4.0	0.20
ZZ-Edge MoS_2-DDT(CH_3)	0.91	0.0	0.00
AC-Edge MoS_2-DDT(SH)	2.31	0.0	0.10
AC-Edge MoS_2-DDT(CH_3)	0.82	0.0	0.00
DDT(SH)-GQD	1.28	0.0	0.00
DDT(CH_3)-GQD	1.32	0.0	0.01
DDT(SH)-GQD(edge)	1.25	0.0	0.01
DDT(CH_3)-GQD(edge)	1.23	0.0	0.00
DDT-DDT(parallel)	0.18	0.0	0.00
DDT-DDT(antiparallel)	0.39	0.0	0.01
DDT(SH)-H_2O	0.23	0.0	0.04
DDT(CH_3)-H_2O	0.07	0.0	0.00
DDT(side)-H_2O	0.04	0.0	0.00

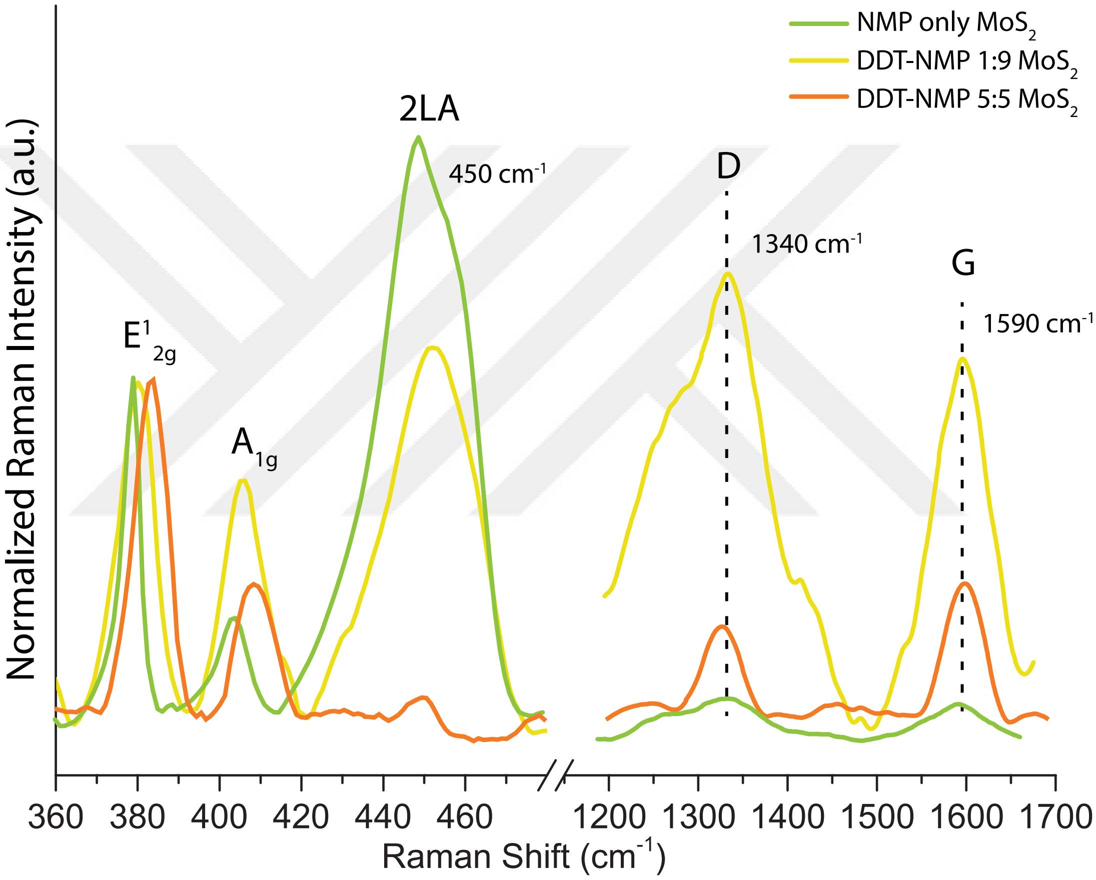

Figure 3.5. The Raman spectra of NMP-MoS_2 and different ratios of DDT-NMP of DDT-MoS_2 functionalized samples on Si/SiO_2 substrates.

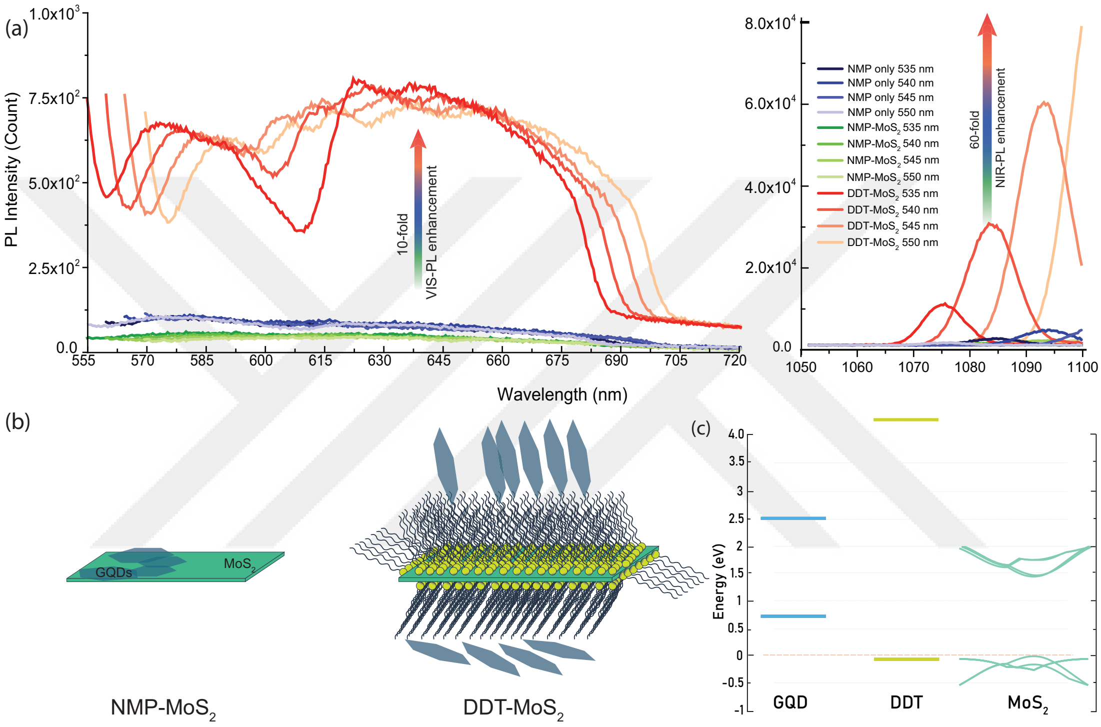

Figure 3.6. (a) Photoluminescence (PL) spectra of the liquid NMP-MoS_2, functionalized DDT-MoS_2 and GQDs samples, excited with 535, 540, 545 and 550 nm wavelengths. (b) Schematic representations of NMP-MoS_2 and DDT-MoS_2 systems. (c) Energy level alignment diagrams for the interface between MoS_2, GQD and DDT in a heterojunction.

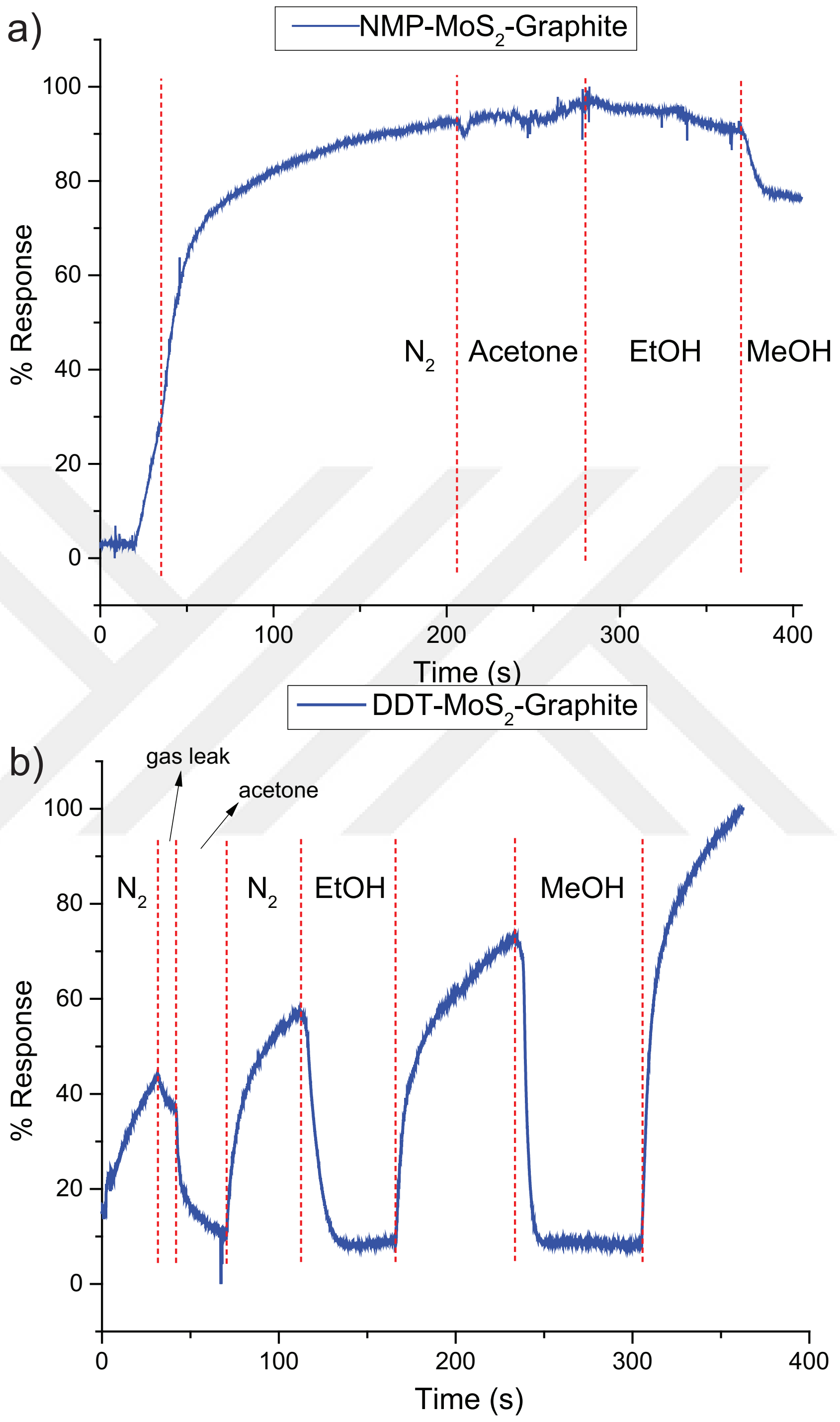

Figure 3.7. Current change of a) NMP-exfoliated MoS_2 and b) DDT-functionalized MoS_2 sensor device when exposed to various organic gases vs. time (s).

CHAPTER 4

ATOMIC-SCALE UNDERSTANDING OF METHANOL-DRIVEN MODULATIONS IN GRAPHENE-BASED CHEMOSENSORS

Graphene produced by the chemical vapor deposition (CVD)[78] and exfoliation[85] method is different from each other in terms of response to volatile organic compound (VOC) gases. It is seen that the experiments with gases such as NO_2[16], NH_3[42] and CO_2[24] exhibit inverse responses with sensing materials which have different methods of synthesis. When exposed to NO_2, Lee et al. found that current response read on a CVD graphene sensor device tends to increase[55]. While in another work by Tammanoon et al., the current read on the sensor device fabricated with exfoliated graphene decreases due to the increase in resistance[88].

While the properties of pristine graphene is very useful for sensing applications, it lacks selectivity towards given targets. In order to increase selectivity of sensing medium, sensor mechanisms consisting of derivatives of graphene structures have been proposed[21]. Past studies in gas sensor field include heterostructures and composites such as graphene-$ZnFe_2O_4$ composite[64], decorated zigzag graphene nanoribbon with copper[4], reduced graphene oxide (rGO)[63], graphene grown on 6H-SiC substrate[54] and transition metal doped graphene[60]. Surfaces exposed to different gases show different responses to the current flowing through the system as p-doped or n-doped[98]. Aforementioned diverseness of responses in graphene makes way for different applications in graphene based sensor devices. Various studies have provided some preliminary information on the sense of VOC molecules such as methanol on graphene, but a complete understanding at the atomic scale has not occurred[53].

Herein, we employ theoretical and experimental methods to understand the reason for the opposite electrical effects on CVD and exfoliated graphene surfaces. The obtained results reveal that the I-V characteristics of CVD and exfoliated graphene are different from each other. However, the sensor responses of CVD and exfoliated graphene against methanol, which are different from each other, have been understood at the atomic scale through first principles calculations.

CVD Graphene Sensor Device Preparation: A solution of 150 mg of poly(methyl

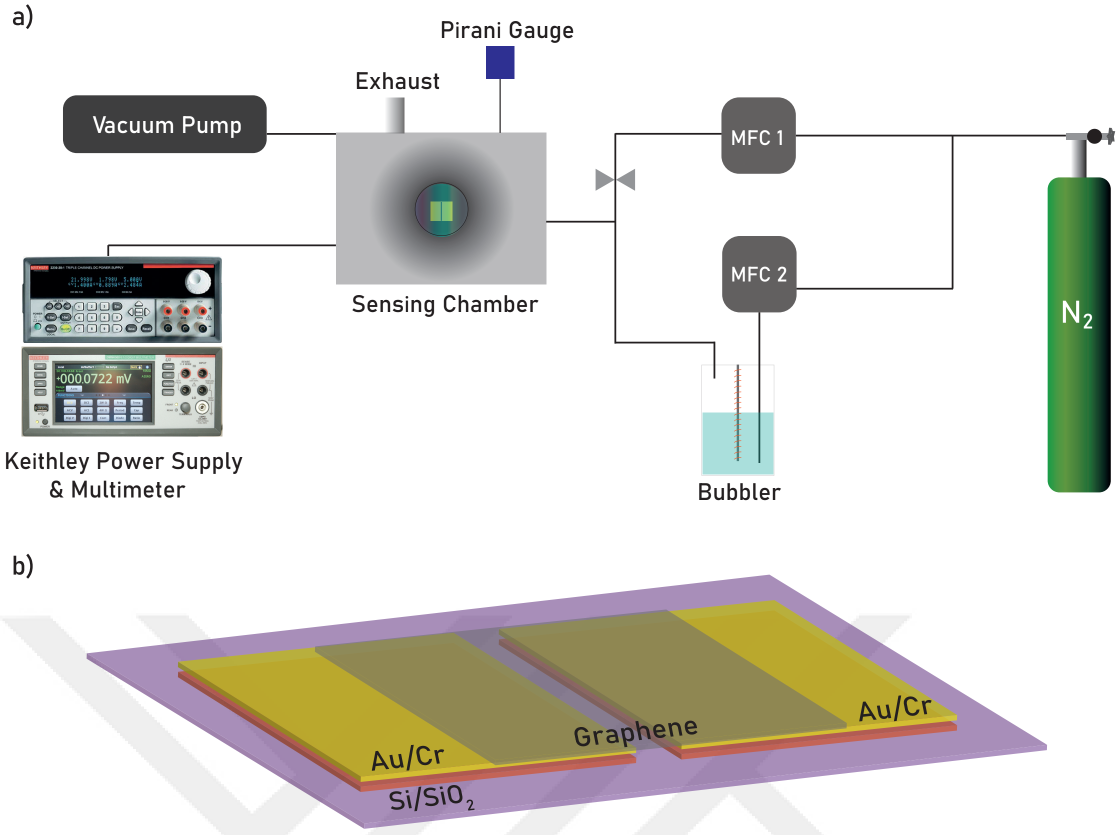

Figure 4.1. (a) Block diagram of the sensor setup and (b) structure of chemiresistor.

methacrylate) (PMMA) in 20 ml of toluene was prepared. The prepared solution was kept overnight in a magnetic stirrer with a magnetic bar. The PMMA solution was dropped on the copper/graphene surfaces and dried in a vacuum oven at 75°C for 2 hours. Then, etching was done in such a way that only graphene and PMMA remained in the prepared acid solution. The remaining PMMA/graphene was kept on the electrode at 70°C and adhered to the electrode surface. It was checked by measuring the resistance that there was a connection on the two surfaces of the electrode.

Exfoliated Graphene Sensor Device Preparation: 2 mg/ml mixture prepared with 20 mg graphite powder and 10 ml N-methyl pyrrolidone (NMP) was sonicated with probe sonicator in an ice bath for 20 minutes (Power 20, pulse 7 s on and 5 s off). After sonication, the resultant mixture from the probe sonicator was stored for 8 hours, then it was centrifuged to acquire the supernatant. (4000 rpm, 2 hours). After exfoliation process, supernatant was dropcast onto the electrode surface and kept in a vacuum oven at 180°C overnight. It was checked by measuring the resistance that there was a connection on the two surfaces of the electrode.

Measuring Response of the Electrodes: Three sets of experiments were per-

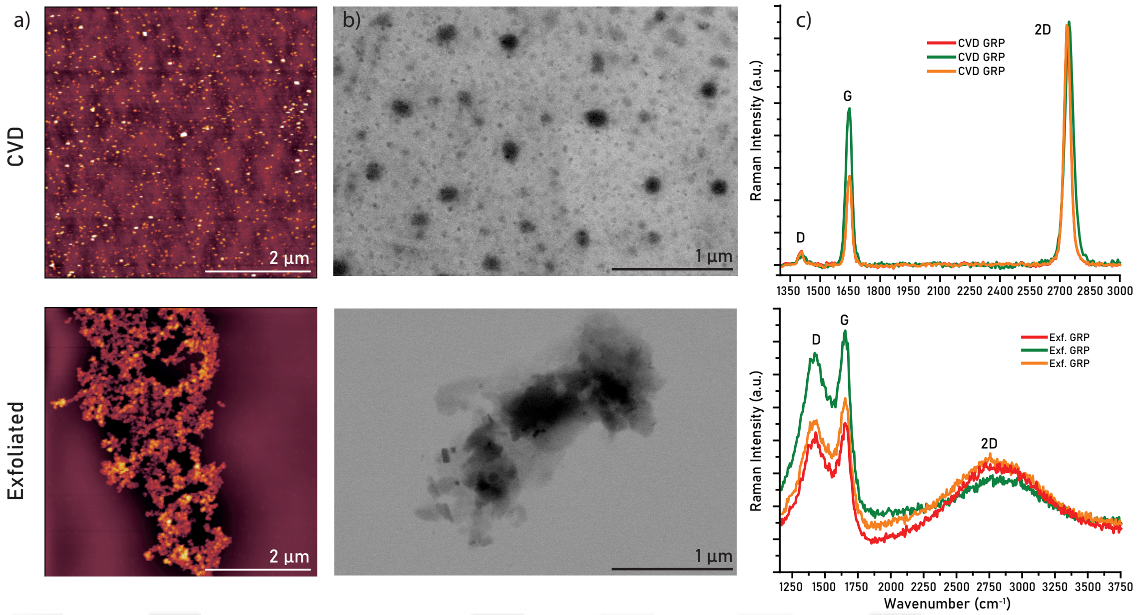

Figure 4.2. AFM images of (a) CVD and (d) exfoliated graphene on Si/SiO$_2$ substrate. STEM images of (b) CVD and (e) exfoliated graphene samples. Raman spectrum of (c) CVD and (f) exfoliated graphene on Si/SiO$_2$ substrate, excited with the laser of 785 nm.

formed for CVD and exfoliated graphene electrodes placed in the sensor mechanism. The sensors were purged with N$_2$ gas for 20 minutes prior to experiment. During the experiment, the device surfaces were exposed to N$_2$ gas for 5 minutes and then to VOC gas for 2 minutes. N$_2$ gas was used as carrier gas in the experiment, which lasted 21 minutes for each VOC. The responses of the surfaces to target gases were recorded.

4.1. Characterization of CVD and Exfoliated Graphene

To study the sensing mechanism responsible for opposite responses of CVD and exfoliated graphene, series of analysis of AFM, STEM and Raman are conducted. For the identification of surface morphology of CVD and exfoliated graphene, AFM measurements are carried out. AFM image of CVD graphene in Fig.4.2a shows a large area of graphene sheets covered with PMMA residues[17]. A close examination of the AFM image reveals that the individual particles have no visible grain boundaries. AFM image of NMP-exfoliated graphene however, shows 65 nm-sized particles in average. The recovered particle size data from AFM measurements of NMP-exfoliated graphene shows much smaller particle sizes than CVD graphene, which also implies greater number of edge sites. The scanning transmission electron microscope (STEM) image is shown in Fig.4.2b. The STEM images

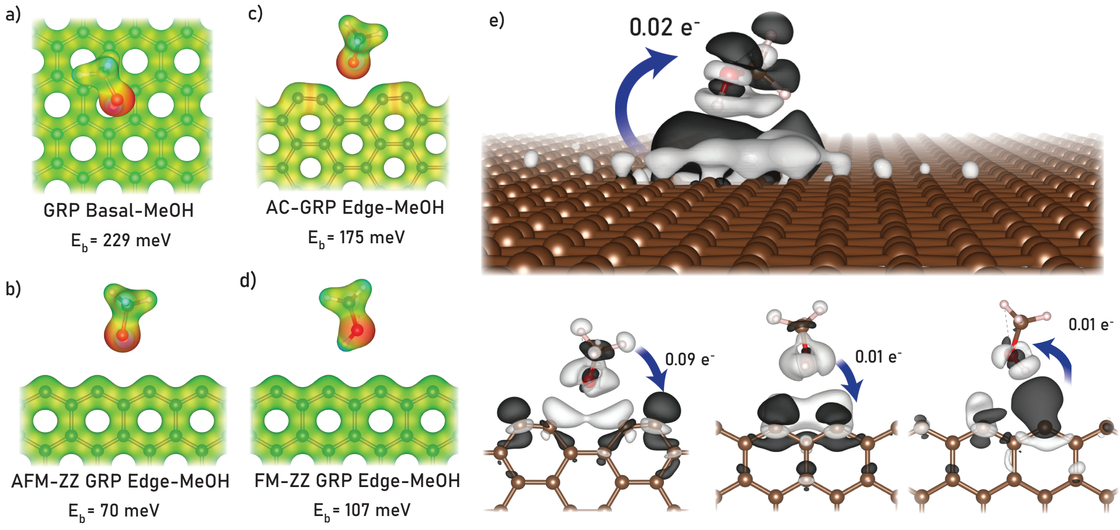

Figure 4.3. Binding energy and electrostatic potential surface of a) basal plane, b) AFM zigzag edge, c) armchair edge and d) FM zigzag edge graphene interactions with methanol molecule. e) Charge density difference and electron transfers upon interaction of methanol and basal plane and edge sites of graphene (positive and negative charge differences are shown with black and white colors, respectively).

of PMMA-covered uniform sheet of CVD graphene is shown in Fig.4.2b. Moreover, NMP-exfoliated graphene sheets are clearly visible, and have sizes of 0.1-1.0 μm on SiO_2/Si substrate. Fig.4.2c shows the Raman spectra of CVD and NMP-exfoliated graphene, respectively. The D ,G and 2D peaks, which appear around 1406 (1419), 1646 (1652) and 2741 (2766) cm^{-1} are prominent Raman lines that can be used to identify the doping characteristics of CVD graphene (NMP-exfoliated graphene), as reported in other studies[28]. Whereas the shift of G band indicates both hole and electron doping[70], the shifting in 2D band indicates only hole doping, as it is reported by Heydrich et al.[40] In this manner, when the Raman spectrum is examined, blue-shifting of 2D band specifically implies p-type doping of both graphene species. Moreover, it is seen that G band of exfoliated graphene blue-shifts about 6 cm^{-1} when compared to CVD graphene which is indicative of higher doping of exfoliated graphene species. Additionally, it is also seen that 2D band of both graphene species blue-shifted. Thus it is concluded that exfoliated graphene is more heavily p-type doped than CVD graphene species.

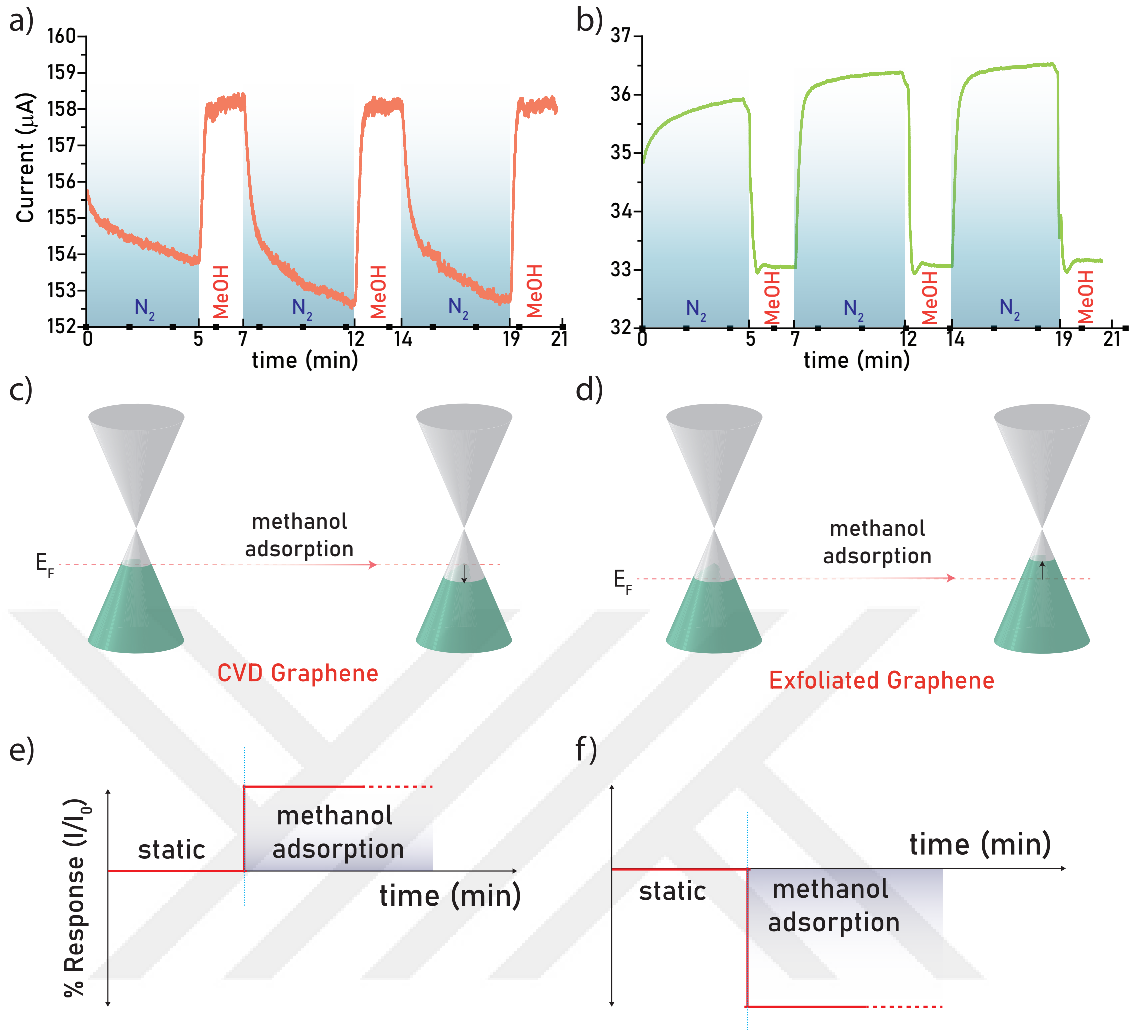

Figure 4.4. Effect of exposure to methanol gas on the normalized current of a) CVD graphene and b) exfoliated graphene chemirestors. Doping level change of c) CVD and d) exfoliated graphene upon exposure to methanol. d) Change of electrical response read on e) CVD and f) exfoliated graphene sensor device due to methanol adsorption.

4.2. Selectivity and Sensitivity Towards VOCs

Whether the sensing material is graphene or not, the basic mechanism in resistive gas sensors is about the electron transfer between sensing material and the analyte. While the electrical features of CVD-grown graphene is well-known and defined, it is still challenging to predict the electrical properties of liquid phase exfoliated graphene. This is due to factors such as oxidation, particle sizes, and involuntary doping that are involved in the experimental media.

All characteristics of CVD and exfoliated graphene aside, the most obvious difference between them is the particle size or, more specifically, the populations of the edge sites. Due to the difference in the electronic properties of the edge site and basal planes of graphene, the properties of CVD and exfoliated graphene differ greatly from each other in the experimental environment.

Although the response time and intensity of the responses can vary due to the binding energy or charge transfer in the system, it is crucial to investigate the electrical properties of the sensing surface and the impacts of the various defects on the sensing media. In Fig.4.3, computational analyzes simulate the sensor surfaces created with the investigated CVD and exfoliated graphene. CVD graphene is modeled as the basal plane of pristine graphene, while edge models of graphene are used to simulate exfoliated graphene surfaces. The different orientations of methanol molecules adsorbed on graphene shown in Fig.4.3 are shown together with electrostatic potential (EPM) maps. Among EPMs, Fig.4.3c, especially armchair edged graphene, appears to be more electronegative than other graphene species. Accordingly, in Fig.4.3e, the charge transfers between the graphene species and the methanol molecule can be seen. In the basal plane (CVD) of graphene, methanol accepts 0.02 e^- from the surface, while when armchair interacts with graphene (exfoliated), methanol donates 0.09 e^- to the graphene surface. The acquired sensor responses of CVD and exfoliated graphene to methanol are shown in Fig.4.4a and b, respectively.

For both graphene species, the periods of sensor measurements were applied as 5 minutes of nitrogen followed by 2 minutes of methanol, as seen in Fig.4.4a,b. At the beginning of the experiment, the surface was exposed to nitrogen gas for 5 minutes before the methanol sensing step, in order to clean the O_2, H_2O and other atmospheric adsorbates adsorbed on the surfaces. After the purging of sensor device, surface is exposed to methanol.

The sensor measurements thus planned are plotted in Fig.4.4a for CVD graphene and Fig.4.4b for exfoliated graphene. The CVD graphene in Fig.4.4a is understood to be a p-type sensor device, both from the measurements we applied with the HPPM method and from the common knowledge in the literature. Accordingly, the doping character of CVD graphene is represented in its Dirac cone and Fig.4.4c, and it is seen that methanol changes the doping level of CVD graphene. According to our charge transfer calculations, basal plane graphene donates 0.02 e^- to the methanol molecule, and accordingly there is a loss of electrons in basal plane of graphene. The loss of electrons in CVD graphene causes the Fermi level of this system to shift down in the energy space, and as a result, the p-type character of the surface increases. Accordingly, it is shown in Fig.4.4e that the current change due to methanol on the sensor surface formed with CVD graphene is positive.

Table 4.1. A data sheet to identify the trend between the sensing mechanisms between different graphene species with MeOH. Binding energies (E_b), amount of electron transfer (ρ), and lastly, the direction in which the electrons will be transferred is shown in the right-end column.

Interaction	**E_b(meV)**	**ρ(e)**	**Direction**
Basal-GRP	229	0.02	GRP → MeOH
AFM-ZZ-GRP	70	0.01	MeOH → GRP
FM-ZZ-GRP	107	0.01	GRP → MeOH
AC-GRP	175	0.09	MeOH → GRP

The main morphological difference of CVD and exfoliated graphene is the redundancy of edge regions in exfoliated samples. Accordingly, electronic effects originating from the edge regions should also be taken into account. Sensor measurements conducted with devices produced with exfoliated graphene are shown in 4.4b. It was determined by HPPM measurements that the exfoliated graphene surfaces were p-type. Accordingly, the doping character of exfoliated graphene is represented in Fig.4.4d with its Dirac cone, and it is seen that methanol also changes the doping level of exfoliated graphene. Sensor devices that are produced with exfoliated graphene has the same type of doping as CVD graphene sensor devices. But contrarily, sensor devices produced with exfoliated graphene showed an inverse response to methanol, when compared to CVD. The reason for the reverse responses from the sensor surfaces is that the basal plane and the edges perform charge transfer in the opposite direction compared to each other with methanol. In the interaction between basal plane graphene and methanol, graphene loses 0.02 e^-, whereas in the interaction between edge plane graphene and methanol, graphene gains 0.09 e^-. Accordingly, it is understood that the Fermi level of the sensor surface shifts up in the energy space and the p-type character decreases in the graphene edge-methanol interaction. Accordingly, it is shown in Fig.4.4f that the current change due to methanol on the sensor surface formed with exfoliated graphene is negative.

To conclude, the opposite electrical effects of methanol on CVD and exfoliated graphene surfaces were investigated. In the experiments performed with the sensor device prepared with CVD graphene, an increase in current was observed as a result of the methanol exposure to the sensor surface. On the contrary, in the experiments performed with the sensor devices prepared with exfoliated graphene, a decrease in current was observed upon methanol exposure. While the p-doping of PMMA-transferred CVD graphene is known, Raman spectroscopy indicate a slightly higher p-doping on exfoliated graphene sensor device by showing a blue-shift at 2D band. Therefore, both of the devices have holes as charge carriers. Moreover, theoretical investigations showed an inverse charge transfer direction on edge site and basal plane of the graphene specie, thus explaining the inverse responses of CVD and exfoliated graphene.

In Fig.4.4a, nitrogen gas flow given in the first step decreases the current value of CVD graphene, while methanol increases it. In the next two sets, the same response is seen stably. On the other hand, in the exfoliated graphene in Fig.4.4b, nitrogen gas increases the current value while methanol decreases the current value. The mechanism by which this situation arises is on the increase or decrease in the densities of charge carriers. In Fig.4.4c and d, it is seen that both CVD and exfoliated graphene surfaces are p-type surfaces. The charge carriers of these surfaces, while the number of hole carriers of graphene increases in calculations made with basal (CVD) graphene, the hole carrier level decreases in calculations made with exfoliated regions. In the simulations made with graphene surfaces, the gas detection mechanisms of the surfaces were understood at the atomic level by the calculations made on the number of electrons gained or lost by the graphene surfaces.

CHAPTER 5

OVERALL DISCUSSION

Overall, motivated by the curious properties of electrons in low-dimensional materials, this master thesis focused on the investigation and the characterization of graphene and 2D MoS_2 that present novel results in terms of morphological, electronic, or optical properties, to comment on gas sensing properties on the materials. The experimental procedure and results were supported with DFT-based first-principles calculations by Vienna ab initio Simulation Package.

Chapter 1 provides an introduction to the thesis and discusses the motivation and objectives.

Chapter 2 explains the experimental methodology, including the wet transfer method of CVD-grown graphene, liquid phase exfoliation, and functionalization of 2D materials. Various characterization techniques such as optical and morphological techniques are also discussed. The theoretical methodology based on density functional theory calculations is explained.

Chapter 3 focuses on the examination of bare exfoliated MoS_2 in NMP and the functionalization process using dodecanethiol. It also discusses the enhancement of sensor response due to DDT-functionalization.

Chapter 4 examines the characterization of CVD and exfoliated graphene and explores their selectivity and sensitivity towards volatile organic compounds (VOCs), particularly methanol.

REFERENCES

(1) Ahmad, R., R. Srivastava, S. Yadav, D. Singh, G. Gupta, S. Chand, and S. Sapra (2017). Functionalized molybdenum disulfide nanosheets for 0d–2d hybrid nanostructures: photoinduced charge transfer and enhanced photoresponse. *The Journal of Physical Chemistry Letters 8*(8), 1729–1738.

(2) Akhavan, O. (2015). Bacteriorhodopsin as a superior substitute for hydrazine in chemical reduction of single-layer graphene oxide sheets. *Carbon 81*, 158–166.

(3) Albersdorfer, A. and S. E. Cross (2007). Principles of atomic force microscopy. *Analytical Chemistry 79*(18), 7169–7177.

(4) Berahman, M. and M. Sheikhi (2015). Hydrogen sulfide gas sensor based on decorated zigzag graphene nanoribbon with copper. *Sensors and Actuators B: Chemical 219*, 338–345.

(5) Bernardi, M., M. Palummo, and J. C. Grossman (2013). Extraordinary sunlight absorption and one nanometer thick photovoltaics using two-dimensional monolayer materials. *Nano letters 13*(8), 3664–3670.

(6) Berne, B. J. and R. Pecora (2000). *Dynamic Light Scattering: With Applications to Chemistry, Biology, and Physics* (2nd ed.). Dover Publications.

(7) Bhushan, B. (2010). *Scanning Probe Microscopy: Principles, Techniques, and Applications* (2nd ed.). Springer.

(8) Blöchl, P. E. (1994). Projector augmented-wave method. *Physical review B 50*(24), 17953.

(9) Brown, D. and E. Lee (2021). *Advanced Gas Sensor Technologies*. ABC Publications.

(10) Chen, J., B. Yao, C. Li, and G. Shi (2012). Anisotropic etching of chemical vapor deposited graphene. *ACS Nano 6*(10), 9944–9952.

(11) Chen, S., J. Zhao, J. Wang, and H. Chen (2016). Applications of dynamic light scattering in the analysis of nanomaterials. *Nano-Micro Letters 8*(3), 187–209.

(12) Chen, X., N. C. Berner, C. Backes, G. S. Duesberg, and A. R. McDonald (2016). Functionalization of two-dimensional mos2: on the reaction between mos2 and organic thiols. *Angewandte Chemie 128*(19), 5897–5902.

(13) Chhowalla, M., H. S. Shin, G. Eda, L.-J. Li, K. P. Loh, and H. Zhang (2013). The chemistry of two-dimensional layered transition metal dichalcogenide nanosheets. *Nature chemistry 5*(4), 263–275.

(14) Chianelli, R., A. Ruppert, S. Behal, B. Kear, A. Wold, and R. Kershaw (1985). The reactivity of mos2 single crystal edge planes. *Journal of Catalysis 92*(1), 56–63.

(15) Cho, K., M. Min, T.-Y. Kim, H. Jeong, J. Pak, J.-K. Kim, J. Jang, S. J. Yun, Y. H. Lee, W.-K. Hong, et al. (2015). Electrical and optical characterization of mos2 with sulfur vacancy passivation by treatment with alkanethiol molecules. *ACS nano 9*(8), 8044–8053.

(16) Choi, H., H. Y. Jeong, D.-S. Lee, C.-G. Choi, and S.-Y. Choi (2013). Flexible no 2 gas sensor using multilayer graphene films by chemical vapor deposition. *Carbon letters 14*(3), 186–189.

(17) Choi, W., M. A. Shehzad, S. Park, and Y. Seo (2017). Influence of removing pmma residues on surface of cvd graphene using a contact-mode atomic force microscope. *RSC advances 7*(12), 6943–6949.

(18) Chou, S. S., M. De, J. Kim, S. Byun, C. Dykstra, J. Yu, J. Huang, and V. P. Dravid (2013). Ligand conjugation of chemically exfoliated mos2. *Journal of the American Chemical Society 135*(12), 4584–4587.

(19) Chou, S. S., B. Kaehr, J. Kim, B. M. Foley, M. De, P. E. Hopkins, J. Huang, C. J. Brinker, and V. P. Dravid (2013). Chemically exfoliated mos2 as near-infrared photothermal agents. *Angewandte Chemie International Edition 52*(15), 4160–4164.

(20) Das, S. K., R. Gawas, S. Chakrabarty, G. Harini, R. Patidar, and K. Jasuja (2019). An unexpected transformation of organic solvents into 2d fluorescent quantum dots

during ultrasonication-assisted liquid-phase exfoliation. *The Journal of Physical Chemistry C 123*(41), 25412–25421.

(21) Dean, C., A. Young, L. Wang, I. Meric, G.-H. Lee, K. Watanabe, T. Taniguchi, K. Shepard, P. Kim, and J. Hone (2012). Graphene based heterostructures. *Solid State Communications 152*(15), 1275–1282.

(22) Dong, H., S. Tang, Y. Hao, H. Yu, W. Dai, G. Zhao, Y. Cao, H. Lu, X. Zhang, and H. Ju (2016). Fluorescent mos2 quantum dots: ultrasonic preparation, up-conversion and down-conversion bioimaging, and photodynamic therapy. *ACS applied materials & interfaces 8*(5), 3107–3114.

(23) Eda, G., H. Yamaguchi, D. Voiry, T. Fujita, M. Chen, and M. Chhowalla (2011). Photoluminescence from chemically exfoliated mos2. *Nano letters 11*(12), 5111–5116.

(24) Fan, X., K. Elgammal, A. D. Smith, M. Östling, A. Delin, M. C. Lemme, and F. Niklaus (2018). Humidity and co2 gas sensing properties of double-layer graphene. *Carbon 127*, 576–587.

(25) Ferraro, J. R. and K. Nakamoto (2003). *Introduction to Raman Spectroscopy* (2nd ed.). CRC Press.

(26) Garcia, M. and W. Chen (2023). Enhanced gas sensing with functionalized mos2. In *Proceedings of the International Conference on Gas Sensing*, pp. 45–56.

(27) Geim, A. K. and K. S. Novoselov (2010). The rise of graphene. In *Nanoscience and technology: a collection of reviews from nature journals*, pp. 11–19. World Scientific.

(28) Giovannetti, G., P. A. Khomyakov, G. Brocks, V. v. Karpan, J. van den Brink, and P. J. Kelly (2008). Doping graphene with metal contacts. *Physical review letters 101*(2), 026803.

(29) Giumlia-Mair, A. (2018). Polychromy on metals in greek and roman times: texts and anal-yses. In *Proceedings of the Workshop Polychromie vor-und frühgeschichtlicher Metallarbeiten: Technische Vielfalt und kulturelle Bedeutung vor-und frühgeschichtlicher Metallarbeiten, Akten des*, Volume 2, pp. 259–273.

(30) Giumlia-Mair, A. (2020). Plating and surface treatments on ancient metalwork. *Advances in Archaeomaterials 1*(1), 1–26.

(31) Goldstein, J. I., D. E. Newbury, D. C. Joy, C. E. Lyman, P. Echlin, E. Lifshin, L. Sawyer, and J. R. Michael (2017). *Scanning Electron Microscopy and X-ray Microanalysis*. Springer.

(32) Gottam, S. R., C.-T. Tsai, L.-W. Wang, C.-T. Wang, C.-C. Lin, and S.-Y. Chu (2020). Highly sensitive hydrogen gas sensor based on a mos2-pt nanoparticle composite. *Applied Surface Science 506*, 144981.

(33) Griffiths, P. and J. de Haseth (2003). *Fourier Transform Infrared Spectrometry* (2nd ed.). Wiley.

(34) Grimme, S., J. Antony, S. Ehrlich, and H. Krieg (2010). A consistent and accurate ab initio parametrization of density functional dispersion correction (dft-d) for the 94 elements h-pu. *The Journal of chemical physics 132*(15), 154104.

(35) Gupta, V., T. S. Sakthivel, and S. Seal (2015). Recent development in 2d materials beyond graphene. *Progress in Materials Science 73*, 44–126.

(36) He, X. and T. Gao (2017). Ultraviolet-visible-near infrared spectroscopy and chemometrics for the non-invasive identification of pigments used in ancient textiles. *Analytical Methods 9*(9), 1382–1389.

(37) Heising, J. and M. G. Kanatzidis (1999). Exfoliated and restacked mos2 and ws2: Ionic or neutral species? encapsulation and ordering of hard electropositive cations. *Journal of the American Chemical Society 121*(50), 11720–11732.

(38) Hellman, H. and R. Feynman (1939). The operator method in quantum mechanics. *Physical Review 56*(7), 340–344.

(39) Hernandez, Y., V. Nicolosi, M. Lotya, F. M. Blighe, Z. Sun, S. De, I. T. McGovern, B. Holland, M. Byrne, Y. K. Gun'Ko, J. J. Boland, P. Niraj, G. Duesberg, S. Krishnamurthy, R. Goodhue, J. Hutchison, V. Scardaci, A. C. Ferrari, and J. N. Coleman (2008). High-yield production of graphene by liquid-phase exfoliation of graphite. *Nature Nanotechnology 3*(9), 563–568.

(40) Heydrich, S., M. Hirmer, C. Preis, T. Korn, J. Eroms, D. Weiss, and C. Schüller (2010). Scanning raman spectroscopy of graphene antidot lattices: Evidence for systematic p-type doping. *Applied Physics Letters 97*(4), 043113.

(41) Hohenberg, P. and W. Kohn (1964). Inhomogeneous electron gas. *Physical Review 136*(3B), B864–B871.

(42) Huang, S., L. A. Panes-Ruiz, A. Croy, M. Löffler, V. Khavrus, V. Bezugly, and G. Cuniberti (2021). Highly sensitive room temperature ammonia gas sensor using pristine graphene: The role of biocompatible stabilizer. *Carbon 173*, 262–270.

(43) Jaramillo, T. F., K. P. Jørgensen, J. Bonde, J. H. Nielsen, S. Horch, and I. Chorkendorff (2007). Identification of active edge sites for electrochemical h2 evolution from mos2 nanocatalysts. *science 317*(5834), 100–102.

(44) Jawaid, A., D. Nepal, K. Park, M. Jespersen, A. Qualley, P. Mirau, L. F. Drummy, and R. A. Vaia (2016). Mechanism for liquid phase exfoliation of mos2. *Chemistry of Materials 28*(1), 337–348.

(45) Kaur, H., M. Shorie, and P. Sabherwal (2020). Biolayer interferometry-selex for shiga toxin antigenic-peptide aptamers & detection via chitosan-wse2 aptasensor. *Biosensors and Bioelectronics 167*, 112498.

(46) Kim, H.-I., D. Yim, S.-J. Jeon, T. W. Kang, I.-J. Hwang, S. Lee, J.-K. Yang, J.-M. Ju, Y. So, and J.-H. Kim (2020). Modulation of oligonucleotide-binding dynamics on ws2 nanosheet interfaces for detection of alzheimer's disease biomarkers. *Biosensors and Bioelectronics 165*, 112401.

(47) Kim, Y., Y. Jhon, J. Park, C. Kim, S. Lee, and Y. Jhon (2016). Plasma functionalization for cyclic transition between neutral and charged excitons in monolayer mos2. *Scientific reports 6*(1), 21405.

(48) Knirsch, K. C., N. C. Berner, H. C. Nerl, C. S. Cucinotta, Z. Gholamvand, N. McEvoy, Z. Wang, I. Abramovic, P. Vecera, and M. Halik (2015). Basal-plane functionalization of chemically exfoliated molybdenum disulfide by diazonium salts. *ACS nano 9*(6), 6018–6030.

(49) Kohn, W. and L. J. Sham (1965). Self-consistent equations including exchange and correlation effects. *Physical review 140*(4A), A1133.

(50) Kresse, G. and J. Furthmüller (1996). Efficient iterative schemes for ab initio total-energy calculations using a plane-wave basis set. *Physical review B 54*(16), 11169.

(51) Kresse, G. and J. Hafner (1993). Ab initio molecular dynamics for liquid metals. *Physical review B 47*(1), 558.

(52) Kumar, R., N. Goel, and M. Kumar (2017). Uv-activated mos2 based fast and reversible no2 sensor at room temperature. *ACS sensors 2*(11), 1744–1752.

(53) Kumar, Y. R., K. Deshmukh, T. Kovářík, and S. K. Pasha (2022). A systematic review on 2d materials for volatile organic compound sensing. *Coordination Chemistry Reviews 461*, 214502.

(54) Lebedev, A., S. Lebedev, S. Novikov, V. Y. Davydov, A. Smirnov, D. Litvin, Y. N. Makarov, and V. Levitskii (2016). Supersensitive graphene-based gas sensor. *Technical Physics 61*(3), 453–457.

(55) Lee, C., J. Ahn, K. B. Lee, D. Kim, and J. Kim (2012). Graphene-based flexible no2 chemical sensors. *Thin Solid Films 520*(16), 5459–5462.

(56) Li, B., J. Cao, X. Wu, Y. Xie, and Z. Liu (2019). Functionalization of two-dimensional mos2: Strategies, synthesis, and applications in energy conversion and storage. *Frontiers in Chemistry 7*, 659.

(57) Li, H., C. Tsai, A. L. Koh, L. Cai, A. W. Contryman, A. H. Fragapane, J. Zhao, H. S. Han, H. C. Manoharan, F. Abild-Pedersen, et al. (2016). Activating and optimizing mos2 basal planes for hydrogen evolution through the formation of strained sulphur vacancies. *Nature materials 15*(1), 48–53.

(58) Li, H., J. Wu, Z. Yin, and H. Zhang (2014). Preparation and applications of mechanically exfoliated single-layer and multilayer mos2 and wse2 nanosheets. *Accounts of chemical research 47*(4), 1067–1075.

(59) Li, Q., Y. Zhao, C. Ling, S. Yuan, Q. Chen, and J. Wang (2017). Towards a comprehensive understanding of the reaction mechanisms between defective mos2 and thiol molecules. *Angewandte Chemie International Edition 56*(35), 10501–10505.

(60) Li, Y., Y. Xu, and X. Li (2022). The sensing mechanism of hcho gas sensor based on transition metal doped graphene: Insights from dft study. *Sensors and Actuators A: Physical 338*, 113460.

(61) Lihter, M., M. Graf, D. Ivekovic, M. Zhang, T.-H. Shen, Y. Zhao, M. Macha, V. Tileli, and A. Radenovic (2021). Electrochemical functionalization of selectively addressed mos2 nanoribbons for sensor device fabrication. *ACS Applied Nano Materials 4*(2), 1076–1084.

(62) Lin, T.-W., N. Dhenadhayalan, H.-L. Lee, Y.-T. Lin, K.-C. Lin, and A. Chang (2019). Fluorescence turn-on chemosensors based on surface-functionalized mos2 quantum dots. *Sensors and Actuators B: Chemical 281*, 659–669.

(63) Lipatov, A., A. Varezhnikov, P. Wilson, V. Sysoev, A. Kolmakov, and A. Sinitskii (2013). Highly selective gas sensor arrays based on thermally reduced graphene oxide. *Nanoscale 5*(12), 5426–5434.

(64) Liu, F., X. Chu, Y. Dong, W. Zhang, W. Sun, and L. Shen (2013). Acetone gas sensors based on graphene-znfe2o4 composite prepared by solvothermal method. *Sensors and Actuators B: Chemical 188*, 469–474.

(65) Liu, T., C. Wang, W. Cui, H. Gong, C. Liang, X. Shi, Z. Li, B. Sun, and Z. Liu (2014). Combined photothermal and photodynamic therapy delivered by pegylated mos2 nanosheets. *Nanoscale 6*(19), 11219–11225.

(66) Liu, Y., R. Ghosh, D. Wu, A. Ismach, R. Ruoff, and K. Lai (2014). Mesoscale imperfections in mos2 atomic layers grown by a vapor transport technique. *Nano letters 14*(8), 4682–4686.

(67) Mei, L., Z. Cao, T. Ying, R. Yang, H. Peng, G. Wang, L. Zheng, Y. Chen, C. Y. Tang, D. Voiry, et al. (2022). Simultaneous electrochemical exfoliation and covalent functionalization of mos2 membrane for ion sieving. *Advanced Materials 34*(26),

2201416.

(68) Mignuzzi, S., A. J. Pollard, N. Bonini, B. Brennan, I. S. Gilmore, M. A. Pimenta, D. Richards, and D. Roy (2015). Effect of disorder on raman scattering of single-layer mo s 2. *Physical Review B 91*(19), 195411.

(69) Najafi, L., B. Taheri, B. Martin-Garcia, S. Bellani, D. Di Girolamo, A. Agresti, R. Oropesa-Nunez, S. Pescetelli, L. Vesce, E. Calabro, et al. (2018). Mos2 quantum dot/graphene hybrids for advanced interface engineering of a ch3nh3pbi3 perovskite solar cell with an efficiency of over 20%. *ACS nano 12*(11), 10736–10754.

(70) Ni, Z. H., H. M. Wang, Z. Q. Luo, Y. Y. Wang, T. Yu, Y. H. Wu, and Z. X. Shen (2010). The effect of vacuum annealing on graphene. *Journal of Raman Spectroscopy: An International Journal for Original Work in all Aspects of Raman Spectroscopy, Including Higher Order Processes, and also Brillouin and Rayleigh Scattering 41*(5), 479–483.

(71) Nicolosi, V., M. Chhowalla, M. G. Kanatzidis, M. S. Strano, and J. N. Coleman (2013). Liquid exfoliation of layered materials. *Science 340*(6139), 1226419.

(72) Novoselov, K. S., A. K. Geim, S. V. Morozov, D.-e. Jiang, Y. Zhang, S. V. Dubonos, I. V. Grigorieva, and A. A. Firsov (2004). Electric field effect in atomically thin carbon films. *science 306*(5696), 666–669.

(73) Park, M. J., S. Gravelsins, J. Son, A. M. Van Der Zande, and A.-A. Dhirani (2019). A scalable, solution-based approach to tuning the solubility and improving the photoluminescence of chemically exfoliated mos2. *ACS nano 13*(6), 6469–6476.

(74) Pennycook, S. J. and P. D. Nellist (2011). Scanning transmission electron microscopy: Imaging and analysis. *Springer Science & Business Media*.

(75) Perdew, J., K. Burke, and M. Ernzerhof (1996a). Generalized gradient approximation made simple. *Physical Review Letters 77*(18), 3865–3868.

(76) Perdew, J. P., K. Burke, and M. Ernzerhof (1996b). Generalized gradient approximation made simple. *Physical review letters 77*(18), 3865.

(77) Reimer, L. and H. Kohl (2008). Transmission electron microscopy: Physics of image formation. *Springer Science & Business Media*.

(78) Ricciardella, F., S. Vollebregt, T. Polichetti, M. Miscuglio, B. Alfano, M. L. Miglietta, E. Massera, G. Di Francia, and P. M. Sarro (2017). Effects of graphene defects on gas sensing properties towards no 2 detection. *Nanoscale 9*(18), 6085–6093.

(79) Roy, S., Y. Bobde, B. Ghosh, and C. Chakraborty (2021). Targeted bioimaging of cancer cells using free folic acid-sensitive molybdenum disulfide quantum dots through fluorescence “turn-off”. *ACS Applied Bio Materials 4*(3), 2839–2849.

(80) Saadati, M., O. Akhavan, and H. Fazli (2021). Single-layer mos2-moo3-x heterojunction nanosheets with simultaneous photoluminescence and co-photocatalytic features. *Catalysts 11*(12), 1445.

(81) Saadati, M., O. Akhavan, H. Fazli, S. Nemati, and H. Baharvand (2023). Controlled differentiation of human neural progenitor cells on molybdenum disulfide/graphene oxide heterojunction scaffolds by photostimulation. *ACS Applied Materials & Interfaces*.

(82) Sarkar, D., X. Xie, J. Kang, H. Zhang, W. Liu, J. Navarrete, M. Moskovits, and K. Banerjee (2015). Functionalization of transition metal dichalcogenides with metallic nanoparticles: implications for doping and gas-sensing. *Nano letters 15*(5), 2852–2862.

(83) Sk, M. A., A. Ananthanarayanan, L. Huang, K. H. Lim, and P. Chen (2014). Revealing the tunable photoluminescence properties of graphene quantum dots. *Journal of Materials Chemistry C 2*(34), 6954–6960.

(84) Smith, E. and G. Dent (2005). Raman spectroscopy: A powerful technique for characterization of semiconducting carbon nanotubes. *IEEE Transactions on Nanotechnology 4*(2), 231–238.

(85) Spasenović, M., S. Andrić, and T. Tomašević-Ilić (2021). Graphene-based chemiresistive gas sensors. In *2021 IEEE 32nd International Conference on Microelectronics (MIEL)*, pp. 25–28. IEEE.

(86) Sui, C., T. Wang, Y. Zhou, H. Yin, X. Meng, S. Zhang, G. I. Waterhouse, Q. Xu, Y. Zhuge, and S. Ai (2019). Photoelectrochemical biosensor for hydroxymethylated dna detection and t4-β-glucosyltransferase activity assay based on ws2 nanosheets and carbon dots. *Biosensors and Bioelectronics 127*, 38–44.

(87) Tabata, H., Y. Sato, K. Oi, O. Kubo, and M. Katayama (2018). Bias-and gate-tunable gas sensor response originating from modulation in the schottky barrier height of a graphene/mos2 van der waals heterojunction. *ACS applied materials & interfaces 10*(44), 38387–38393.

(88) Tammanoon, N., A. Wisitsoraat, C. Sriprachuabwong, D. Phokharatkul, A. Tuantranont, S. Phanichphant, and C. Liewhiran (2015). Ultrasensitive no2 sensor based on ohmic metal–semiconductor interfaces of electrolytically exfoliated graphene/flame-spray-made sno2 nanoparticles composite operating at low temperatures. *ACS applied materials & interfaces 7*(43), 24338–24352.

(89) Tan, C., X. Cao, X.-J. Wu, Q. He, J. Yang, X. Zhang, W. Zhao, S. Han, G.-H. Nam, M. Sindoro, and H. Zhang (2017). Recent advances in ultrathin two-dimensional nanomaterials. *Chemical Reviews 117*(9), 6225–6331.

(90) Taylor, M. (2020). Development and characterization of graphene-mos2 gas sensor.

(91) Tilmann, R., C. Weiß, C. P. Cullen, L. Peters, O. Hartwig, L. Höltgen, T. Stimpel-Lindner, K. C. Knirsch, N. McEvoy, A. Hirsch, et al. (2021). Highly selective non-covalent on-chip functionalization of layered materials. *Advanced Electronic Materials 7*(7), 2000564.

(92) Voiry, D., A. Goswami, R. Kappera, C. d. C. C. e Silva, D. Kaplan, T. Fujita, M. Chen, T. Asefa, and M. Chhowalla (2015). Covalent functionalization of monolayered transition metal dichalcogenides by phase engineering. *Nature chemistry 7*(1), 45–49.

(93) Voiry, D., J. Yang, and M. Chhowalla (2016). Recent strategies for improving the catalytic activity of 2d tmd nanosheets toward the hydrogen evolution reaction. *Advanced materials 28*(29), 6197–6206.

(94) Wang, T., H. Zhu, J. Zhuo, Z. Zhu, P. Papakonstantinou, G. Lubarsky, J. Lin, and M. Li

(2013). Biosensor based on ultrasmall mos2 nanoparticles for electrochemical detection of h2o2 released by cells at the nanomolar level. *Analytical chemistry 85*(21), 10289–10295.

(95) Williams, D. B. and C. B. Carter (2009). *Transmission Electron Microscopy: A Textbook for Materials Science* (2nd ed.). Springer.

(96) Wilson, S. and A. Thomas (2021). Gas sensing performance of graphene-mos2 heterostructures. *Journal of Nanotechnology 15*(2), 67–78.

(97) Xia, Y., C. Hu, S. Guo, L. Zhang, M. Wang, J. Peng, L. Xu, and J. Wang (2019). Sulfur-vacancy-enriched mos2 nanosheets based heterostructures for near-infrared optoelectronic no2 sensing. *ACS Applied Nano Materials 3*(1), 665–673.

(98) Xie, T., Q. Wang, R. M. Wallace, and C. Gong (2021). Understanding and optimization of graphene gas sensors. *Applied Physics Letters 119*(1), 013104.

(99) Yamazoe, N. (2005). Toward innovations of gas sensor technology. *Sensors and Actuators B: Chemical 108*(1-2), 2–14.

(100) Yang, J.-K., H.-R. Lee, I.-J. Hwang, H.-I. Kim, D. Yim, and J.-H. Kim (2018). Fluorescent 2d ws2 nanosheets bearing chemical affinity elements for the recognition of glycated hemoglobin. *Advanced healthcare materials 7*(14), 1701496.

(101) Zeng, S., S. Hu, J. Xia, T. Anderson, X.-Q. Dinh, X.-M. Meng, P. Coquet, and K.-T. Yong (2015). Graphene–mos2 hybrid nanostructures enhanced surface plasmon resonance biosensors. *Sensors and Actuators B: Chemical 207*, 801–810.

(102) Zhang, W., J. Du, Z. Liu, D. Zhang, Q. Wei, H. Liu, W. Ma, W. Ren, and H.-M. Cheng (2019). Production of carbon dots during the liquid phase exfoliation of mos2 quantum dots. *Carbon 155*, 243–249.

(103) Zhang, Y., D. Feng, Y. Xu, Z. Yin, W. Dou, U. E. Habiba, C. Pan, Z. Zhang, H. Mou, and H. Deng (2021). Dna-based functionalization of two-dimensional mos2 fet biosensor for ultrasensitive detection of psa. *Applied Surface Science 548*, 149169.

(104) Zheng, F., Z. Wei, H. Xia, Y. Tu, X. Meng, K. Zhu, J. Zhao, Y. Zhu, J. Zhang, Y. Yang,

et al. (2022). 3d mos2 foam integrated with carbon paper as binder-free anode for high performance sodium-ion batteries. *Journal of Energy Chemistry 65*, 26–33.